REVIEW

Check for updates

Measurement, interpretation, and application of electrochemical impedance spectroscopy to lithium-ion batteries

Yuhao Zhang,[a] Jiayuan Xu,[a] Xinyi Xie,[a] Qiu-An Huang,*[b] Shijie Cheng[a] and Jia Xie [ID] *[a]

With the widespread application of lithium-ion batteries, thermal safety and state monitoring have emerged as critical issues that hinder the advancement of high-energy-density battery systems. Faced with the above challenges, multidimensional sensing technologies such as gas, pressure, temperature, imaging, and sound have been explored for critical alerts. But the effect is not satisfactory. For instance, traditional temperature sensing technologies, constrained by localized measurement hysteresis and insufficient spatial resolution, struggle to rapidly and in real-time capture the dynamic evolution of internal thermal anomalies in batteries. In contrast, electrochemical impedance spectroscopy (EIS) serves as a non-invasive diagnostic technique that elucidates internal electrochemical–thermal coupling mechanisms through frequency response analysis. This approach paves the way for innovative paradigms in thermal state monitoring and health management of lithium battery systems. The present paper systematically reviews the latest advancements in EIS technologies pertaining to battery safety, focused on analyzing innovations in impedance measurement chips and devices, impedance data processing algorithms, and impedance-based intelligent applications. Our primary objective is to promote the implementation and widespread adoption of high-reliability, low-cost battery management systems utilizing alternating current (AC) impedance.

Broader context

As the global energy system undergoes an unprecedented transition toward electrification, lithium-ion batteries have emerged as a critical technology for integrating renewable energy and enabling electric mobility. This energy transition has exposed key flaws in existing battery safety frameworks, as traditional monitoring methods are unable to effectively address the complex interplay between electrochemical kinetics and thermodynamics under large-scale conditions. Different from traditional single-temperature sensing, Electrochemical Impedance Spectroscopy (EIS) enables timely warnings of safety issues because it provides wide-band and high-precision kinetic information from bulk to interfaces. The emergence of chip-level EIS measurement solutions and impedance deconvolution technologies based on DRT is driving a shift in safety measures from reactive responses to a predictive battery health ecosystem. These advancements have profound implications for expanding secondary battery applications, optimising fast-charging protocols, and achieving safe battery architectures.

1. Introduction

The global energy infrastructure is at a critical juncture, facing the challenges of surging electricity demand and increasingly severe environmental pollution issues. Although fossil fuels still dominate the current primary energy supply, related

[a]*State Key Laboratory of Advanced Electromagnetic Engineering and Technology, School of Electrical and Electronic Engineering, Huazhong University of Science and Technology, Wuhan 430074, P. R. China. E-mail: ziqizeng@hust.edu.cn, xiejia@hust.edu.cn*
[b]*Faculty of Physics/College of Sciences, Shanghai University, Shanghai 200444, P. R. China. E-mail: hqahqahqa@163.com*

carbon neutrality regulations and policies have significantly spurred an unprecedented expansion of renewable energy.[1,2] Meanwhile, the levelized cost of electricity (LCOE) for solar and wind power is gradually decreasing, coupled with rapid breakthroughs in energy storage technology, enabling renewable energy projects to achieve scalable profitability for the first time. As a result, global green capital is rapidly converging towards the renewable energy sector.[3]

With the rapid development of new energy technologies, lithium-ion batteries, as the current representative energy storage medium, have seen substantial expansion in both demand scale and application scenarios.[4–6] Although the battery systems demonstrate excellent performance metrics in terms of

energy/power density,[7] cycle life,[8] and capacity retention,[9] the thermal safety issues under different operating conditions,[10] particularly the severe consequences induced by thermal runaway,[11] impose more stringent technical requirements on the accompanying safety management systems. For practical applications, current energy storage systems have established a multimodal collaborative safety monitoring framework, utilizing information such as temperature, pressure, gas, SOC, and crack formation as early warning indicators, supplemented by multidimensional sensing technologies.[12–14] Usually, Battery Management Systems (BMSs) can effectively prevent and provide early warnings for safety risks due to mechanical and electrical abuse by means of electrical signal-based voltage monitoring, over-voltage protection, current limiting, balancing, and disconnection.[15–18] However, there is currently no highly reliable method to provide safety warnings for thermal abuse.[11,19] The problem of thermal abuse has become increasingly severe due to significant temperature differences between the inside and outside of the battery, which are not only difficult to monitor but also have hysteresis effects. Moreover, common temperature monitoring methods struggle to balance cost and efficiency. Thermistors are low-cost but have a slow thermal response and limited accuracy; thermocouples provide high-precision measurements and have a rapid thermal response, but they are expensive and susceptible to noise interference;[20] resistance temperature detectors (RTDs) face challenges such as large size and manufacturing difficulties. New temperature sensing techniques, such as Fiber Bragg Grating (FBG) sensors,[21–23] in spite of being compact and potentially integrable within the battery, still face considerable challenges regarding feature analysis and the onboard application of optical signals. Furthermore, conventional monitoring of voltage, current, and even pressure and gas offers limited assistance for real-time temperature monitoring.

In contrast, the impedance characteristics of batteries exhibit a strong correlation with temperature over a wide temperature range. In most thermal abuse scenarios, the changes in relevant impedance characteristics are notably pronounced and generally occur earlier than the onset of thermal runaway. In addition, within the battery module, issues such as connector aging,[24] contamination,[25] and looseness can be monitored through DC resistance measurements, while problems like battery aging, localized lithium plating, and electrolyte corrosion can be evaluated through AC impedance measurements. Due to the need for a certain amplitude of current in DC resistance measurement, it can also be equivalently represented by AC impedance around 1 kHz, thus standardizing DC resistance acquisition into AC impedance measurement. It is essential to emphasize that, given the current trend of increasing capacity in individual battery cells, the welding impedance between the cell and the tab has become comparable to the internal resistance of the battery unit itself, and the safety risks from the connection should not be ignored.

In summary, the current temperature sensors and the associated integration challenges pose an urgent need for non-invasive thermal safety monitoring methods.[26] Faced with the above demands, Electrochemical Impedance Spectroscopy

(EIS) might provide a new approach, not only for temperature detection inside batteries but also for other safety monitoring of batteries.[27] EIS has attracted increasing attention in evaluating electrode performance, diagnosing kinetic mechanisms, and monitoring the operating state of LIBs. Therefore, review articles on battery impedance continue to emerge. These reviews are mainly concentrated on the following aspects.

(1) Fundamental concepts. Orazem et al. presented EIS as a transfer function technique applied to electrochemical systems.[28] Lazanas et al. gave a tutorial for EIS from the theoretical background, the principles, and applications in detail.[29]

(2) Theoretical models. Single et al. took planar electrodes as an example to derive a physics-based impedance model in which a SEI is considered.[30] Chen et al. also reviewed how to model porous electrodes and how to apply the developed models to LIBs.[31]

(3) Fast measurement. Wang et al. reviewed the impedance measurement for onboard battery management.[32]

(4) Typical applications. Mc Carthy et al. reviewed how to use EIS to estimate SOC, SOH, and temperature for LIBs.[33] Qu et al. briefly reviewed how to probe process kinetics using EIS of batteries.[34] Iurilli et al. reviewed how to characterize and model the aging phenomena using EIS of LIBs.[35] Hu et al. gave a critical review on rapidly developing impedance techniques for degradation and aging investigation of LIBs.[36]

(5) Broad range introductions. Concentrated on EIS, Vivier et al. systematically reviewed model development, measurement model analysis, and model interpretation in terms of the proposed reaction mechanism.[37] Du et al. reviewed impedance definition, impedance acquisition, impedance analysis, and impedance application for LIBs.[38] Meddings et al. critically assessed impedance measurement, calibration, interpretation, validation, and equivalent circuit models, all of which are applied to commercial LIBs.[39]

Although there are abundant literature reviews on impedance spectroscopy, most of them were focused on basic concepts, theoretical models, rapid testing, typical applications, and broad range introductions. Up to now, there is a lack of a systematic review on testing methods, testing safety, testing nonlinearity, data validation, and data interpretation. The above contents are the premise and foundation in impedance data-driven battery safety monitoring and intelligent diagnosis. In view of this, this work reviews the technological closed-loop of innovative impedance applications from measurement to processing to implementation. In detail, this work reviews these technological frontiers as follows:

(1) Classify various impedance measurement methods and devices, focusing on two mass-produced impedance measurement chips, and analyze their application prospects.

(2) Review recent advancements in impedance data acquisition, validation and interpretation, and evaluate the applicability and inherent technical limitations of various methodologies.

(3) Discuss impedance-based safety management such as SOC/SOH monitoring and temperature estimation, and investigate physics-informed thermal models and data-driven neural networks.

2 Measurement of impedance spectra

2.1 Basic knowledge of impedance measurement

Due to the strongly nonlinear and time-varying characteristics of lithium-ion batteries (LIBs), small-signal perturbation is commonly employed for AC impedance measurement. By applying small-amplitude multi-frequency AC excitation signals[40] near the operating point, the system response satisfies the fundamental assumptions of causality (response solely caused by excitation), linearity (response approximately proportional to excitation), stability and boundedness (finite excitation energy and bounded response frequency range). Under these conditions, the battery's voltage or current response is measured synchronously. To express the impedance concept with the imposed time-domain excitation and response signals, the complex phasor method is typically employed. *Via* Fourier transform analysis at the specific frequency ω, the AC current excitation and voltage response signals are converted into their complex phasor representations: $\Delta \dot{I}(j\omega) = I e^{j\phi_i}$ and $\Delta \dot{U}(j\omega) = U e^{j\phi_u}$ where I and U represent the magnitudes, and ϕ_i and ϕ_u denote their respective phase angles. The complex impedance at frequency ω is then calculated from the ratio of these phasors:

$$Z(j\omega) = \frac{\Delta \dot{I}(j\omega)}{\Delta \dot{U}(j\omega)} = \frac{I e^{j\phi_i}}{U e^{j\phi_u}}. \tag{1}$$

This formula directly provides both the magnitude and phase information of the complex impedance $Z(j\omega)$, enabling the construction of detailed Nyquist plots for battery characterization. These plots effectively capture the kinetics of charge transfer reactions and conform to the causal constraints required by the Kramers–Kronig relations, thereby providing a reliable basis for the non-destructive evaluation and diagnosis of LIBs.

The typical impedance measurement is primarily sorted into two modes based on excitation signals: galvanostatic (constant current) and potentiostatic (constant potential). In large-scale battery modules, the galvanostatic mode is predominantly adopted due to advantages in current control stability and ease of realization.[41] The predominant perturbation signal in EIS measurement is single-frequency sinusoidal excitation, whose key advantage lies in its highly concentrated power spectral density enabling a superior signal-to-noise ratio (SNR) and inherent noise rejection. However, it suffers from prolonged measurement durations and strong dependency on DAC module precision during waveform generation. To reduce the EIS measurement period and simplify excitation signal generation, the research focus has shifted from frequency sweep to novel strategies including multi-sine, multi-pulse, step signals, PRBSs[42] and so on. These approaches leverage time-frequency domain transformations to achieve parallel multi-frequency high-gain measurements with optimized noise suppression. The characteristics and implementation of

these innovative methods will be discussed in detail in the subsequent sections.

Besides, the typical Nyquist plot of LIBs usually exhibits four characteristic regions from high to low frequencies, *i.e.* parasitic inductance, SEI medium, charge transfer and solid–liquid diffusion, respectively. In the high-frequency region, the intersection with the real axis can be quantified as ohmic resistance, which includes contributions from electrolyte ionic conductivity, current collector contact, and separator resistance. The mid-to-high frequency semicircle represents the impedance of the solid-electrolyte interphase (SEI). A stable SEI layer manifests as a small, consistent semicircle, while repeated cycling often enlarges this feature due to SEI thickening or crack formation. In the mid-to-low frequency range, the semicircle corresponds to charge transfer resistance at the electrode surface. A larger semicircle diameter suggests sluggish reaction kinetics, which may stem from degraded active materials, insufficient electrolyte wetting, or reduced catalytic activity.[43] At the lowest frequencies, the inclined line reflects lithium-ion diffusion dynamics. This region is sensitive to the particle size, porosity, solid/electrolyte diffusion coefficient, and ion transfer number, with deviations in slope often indicating inhomogeneous diffusion or phase separation.[44,45]

2.2 Challenges of impedance measurement

The effectiveness of EIS modules in analyzing LIBs relies on their ability to perform long-term measurements accurately. However, module-level implementation faces four major challenges: inter-cell crosstalk causing signal contamination, DC bias-induced nonlinear distortion in measurements, contact resistance compromising impedance data reliability, and high-frequency noise from advanced excitation signals degrading measurement accuracy.[46] Whether adopting a centralized or distributed architecture, inherent trade-offs involving cost, complexity, robustness, and measurement bandwidth must be considered when addressing these issues. Each system configuration presents specific limitations: centralized systems are prone to DC bias and contact resistance effects, whereas distributed systems[47] may encounter constraints in excitation signal amplitude, crosstalk interference, and increased costs.[48] Furthermore, under dynamic operating conditions, additional polarization interference can arise, necessitating high-precision synchronous acquisition techniques to isolate artifacts and ensure measurement accuracy.[49]

L. H. J. Raijmakers *et al.* and NXP Semiconductors[50] noted this issue over time, revealing the crosstalk interference mechanism in multi-cell synchronous impedance measurements of battery packs (*i.e.* higher crosstalk at higher frequencies) through experimental and modeling approaches. This crosstalk originates from electromagnetic coupling between cells and can be expressed using the transfer function $H_{22}^*(j\omega) = H_{22}(j\omega) + H_{21}(j\omega)I_1(j\omega)/I_2(j\omega)$, which is very similar to the mutual inductance between coils. Importantly, their research also showed that crosstalk impedance is independent of battery temperature and SOC, simplifying both modelling and compensation. To address crosstalk, the perturbation fre-

quencies of adjacent cells can be set to slightly different values. However, this prolongs the overall measurement period and is typically only applicable to distributed EIS systems.[48] Although most EIS systems could eliminate crosstalk components by embedding transfer function matrices in impedance algorithms, it remains challenging to obtain such matrices in multi-cell coupling scenarios.[50,51]

The DC bias in impedance measurements fundamentally manifests as an external representation of system nonlinearity, arising from dynamic coupling between operating current and perturbation signals.[46,52,53] Experimental results suggest that when the DC component exceeds fivefold the AC perturbation amplitude ($I_{dc}/I_{ac} > 5$), it induces significant Warburg impedance distortion (low-frequency phase angle deviation up to ±7°).[54] This effect is particularly pronounced during the discharge, exhibiting impedance variation rates 2–3 times higher than charging states.[54] To better compensate/reject the DC bias effect, the nonlinear decay characteristics of the Li-ion diffusion coefficient D_{Li^+} need to be considered, along with a compensation formula that takes into account the enhancement of concentration polarisation coupled with harmonic mixing.

Whether using laser welding or ultrasonic welding, it relies on the contact resistance between busbars and battery terminals/tabs. In EIS measurement systems, only the approach to solder the FPC flexible circuit boards close to the battery tabs (clamped between collector bars and battery lugs) can be considered virtually free from contact resistance effects. These contact resistances from common welding methods have been extensively reported and are summarized in Table 1, where they are compared in magnitude to the ohmic resistance of high-capacity batteries. The contact resistance of connectors may vary with pressure during soldering, contact area, and surface roughness. It can also increase as a result of fatigue caused by continuous vibration. Usually, it is difficult to predict these variations. Currently, they are roughly classified as components of ohmic resistance or as components of resistive/inductive coupled interference. A uniform mean compensation is usually applied during impedance measurements according to the following formula:

$$\text{Re}(Z)_{comp} = \text{Re}(Z)_{meas} + M_{re} \cdot f + R_{par} \quad (2)$$

$$\text{Im}(Z)_{comp} = \text{Im}(Z)_{meas} + M_{im} \cdot f + I_{par}. \quad (3)$$

In the above contact resistance correction for EIS measurement, $\text{Re}(Z)_{comp}$ and $\text{Im}(Z)_{comp}$ denote the corrected real and imaginary parts, respectively; $\text{Re}(Z)_{meas}$ and $\text{Im}(Z)_{meas}$ represent the measured real and imaginary parts, respectively; M_{re} and M_{im} are the inductive compensation coefficients for the real and imaginary parts, respectively; f is the frequency; and R_{par} and I_{par} are the resistive compensation terms for the real and imaginary parts,[47] respectively.

Finally, multi-sine perturbation and PRBS methods have become integral components of contemporary battery AC impedance measurement techniques, offering significant improvements in both speed and accuracy for impedance spectra. These approaches are particularly valuable for on-board and real-time applications where conventional frequency-sweep methods are impractical due to time constraints. A multi-sine signal can typically be expressed as:

$$x[\text{k}] = \sum_{n=1}^{N_f} A_n \cos(2\pi f_0 k \delta t + \varphi_n). \quad (4)$$

The superimposed multi-sine configuration maintains a relatively uniform power distribution across the frequency points of interest, resulting in lower noise amplification. Although multi-sine perturbation signals are gaining increasing recognition, the superposition of multiple signals may induce nonlinear distortion, which results in technical challenges in signal generation. To achieve better results, Kallel and Kanoun's multi-sine method enhances measurement performance by 78% time reduction (from 1440 s to 315 s) and 84% stability improvement (from 201.21 ppm to 31.70 ppm) through frequency/crest factor optimization.[58] This method holds significant practical implications because it improves the stability of multi-sinusoidal impedance measurement by introducing a virtual excitation time interval that merely disturbs with no measurement under dynamic conditions, replacing the original static relaxation time. In addition, optimization methods for multi-sine perturbation signals also include the evolutionary role-playing game theory (ERPGT) based phase optimization,[58] the crest factor optimization using the bee swarm algorithm,[59] and the genetic algorithm-based phase optimization.[60] These advanced computational methods have substantially improved the performance of multi-sine measurements, making them particularly suitable for centralized EIS applications (Fig. 1).[61]

Compared to multi-sine signals, PRBSs exhibit an approximately uniform power spectral density over the measured frequency range and have some high-frequency harmonic gain beyond the measurement band, thereby resulting in increased intrinsic noise and complexity in design/decoding signals. In spite of the above challenges, advantages such as hardware compatibility and multi-frequency acquisition make them one of the most important research directions for fast impedance measurement. Related technological innovations include third-order ternary sequences,[62] which improve low-frequency performance while reducing injection amplitudes; discrete interval binary sequences (DIBSs)[42] that eliminate spectral

Table 1 Comparison between the contact resistance of common soldering methods and the ohmic resistance of high-capacity batteries

Type	Method	Resistance
Welding	Resistance spot welding[55]	0.167 mΩ
	Ultrasonic welding[55]	0.169 mΩ
	Laser beam welding[55]	0.130 mΩ
	Soldering[55]	0.080 mΩ
	Ultrasonic welding[56]	0.250 mΩ
	Press contact(min)[57]	0.050 mΩ
Battery	LF304 EVE energy 304 A h	≤0.160 mΩ
	LF160 EVE energy 160 A h	≤0.210 mΩ

Fig. 1 Schematic of the impedance spectra of LIBs based on small-signal perturbation measurement.[36]

Fig. 2 Four challenges of impedance measurement.

leakage and amplify target frequency energy by 4–8 times; and post-processing algorithms incorporating filtering techniques such as Gaussian filters,[63] moving average filters[63] and so on. In order to speed up the practical implementation of PRBSs, a unified evaluation framework is urgently required for these technological innovations.

Fig. 2 gives a brief summary of section 2.2.

2.3 Impedance measurement methods

This section summarizes various AC impedance measurement methods and the corresponding devices for lithium-ion batteries. Compared with specialized laboratory electrochemical workstations, these devices exhibit lower cost, faster measurement, higher portability, and better compatibility with BMS architectures, though with generally slightly inferior accuracy. These methods are divided into two categories: centralized EIS and distributed EIS.

2.3.1 Centralized EIS. The centralized EIS system exhibits significant advantages due to their robust perturbation current, which help to effectively capture impedance characteristics related to high-capacity lithium batteries. These systems also achieve the comparison of internal consistency of batteries by current amplitudes maintained at a uniform level. However, the centralized EIS system is susceptible to inter-
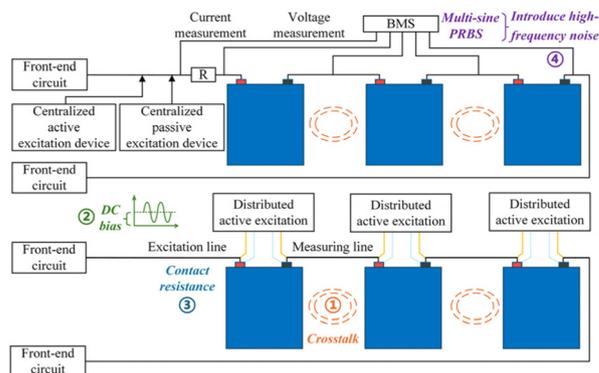
ference from external noise signals. Currently, research studies mainly focus on vehicle applications, and given the prevalent implementation of front-end DC–DC/DC–AC circuits, more investigations target passive excitation perturbation under various circuit configurations. Table 2 summarizes relevant methods and devices for centralized EIS measurement.

The current research mainly focuses on electric vehicle charger OBCs, electric vehicle front-end DC–DC converters, and DC–AC inverters under three-phase motor backgrounds, with the corresponding passive excitation AC impedance measurement introduction schemes designed, which matches well the actual battery peripheral circuit situation. The related scheme incurs almost no additional cost, as it can be implemented using an existing DSP controller and BMS. However, switching tube-based PWM control strategies for generating the perturbation signal also produce triangular wave noise approximating half of the switching frequency, which is inherently present in the circuit while simultaneously imposing restrictions on the highest-frequency disturbances. For application scenarios, switching frequencies of 10 kHz, 20 kHz, and 40 kHz correspond to the possible limiting disturbance frequencies of 2 kHz, 4 kHz, and 8 kHz, or even lower.[69]

Next, the three scenarios of electric vehicle charger OBCs, electric vehicle front-end DC–DC converters, and DC–AC inverters are discussed separately. (i) For the on-board charger, the introduction of excitation signals can help monitor the overcharging of batteries. However, a large charging current bias requires compensation of the measured low-frequency impedance in order to achieve a high-precision impedance measurement. (ii) For the front-end converter, the introduction of excitation signals can help to enhance dynamic thermal management for batteries. But due to power fluctuations, excitation signals need to be accelerated and a certain rest time should be reserved in order to achieve a high-precision impedance measurement for batteries. (iii) For the three-phase motor, the introduction of impedance measurement needs to ensure no impact on motor torque and electromagnetic power. Due to the nonlinearity caused by motor magnetic saturation, low-frequency excitation disturbances require larger currents, which bring larger AC ohmic losses while also requiring

Table 2 A summary of centralized EIS methods and devices

| Front-end circuit	Control algorithm	Range/amplitude	Time	Error	Battery
TAB DC–DC	Phase shift control[64]	0.1–200 Hz/20 A	—	—	350 V pack 2p
DAB	PI/closed-loop[65]	0.1–500 Hz/2 A	—	RMSE 4%	8 A h 6s1p
Boost	ACMC/DIBS[66]	0.1 Hz–1 kHz/100 mA	—	±1.7%	1.2 A h/2 A h
DC–DC	Step/DFT[67]	10 Hz–9 kHz/0.2 C	—	<3%	2.6 A h 3s1p
DC–DC	Multi-sine/FIBC[61]	0.1 Hz–1 kHz/0.75 A	150 s	<3.2%	150 W Fuel cell
DC–DC	FFT[68]	0.1 Hz–5 kHz/5 A	81 s	5.6 mΩ	40 A h 3s1p
PCC DC–DC	PI + PR/closed-loop[69]	1 Hz–2 kHz/2 A	—	—	Fuel cell stack
DC—DC	Three-level/PI[70]	0.1 Hz–2 kHz/0.4 A	—	—	20 A h 6s1p
DC–DC	Interleaved converter[71]	0.1–100 Hz/0.1 A	—	3.85%	9 A h 12 V
DC–DC	DP control[72]	0.1 Hz–25 kHz/50 mA	59.2 s	1.61%	3.35 A h
Full-bridge	DRBS/FFT[73]	0.1–800 Hz/0.1 C	10.13 s	≈3.5%	3.5/10/50 A h
Full-bridge	Phase shift/dual-loop[74]	0.1 Hz–1 kHz/—	—	—	48 V 365 A h
DC–AC	Dual d/q decouple[75]	0.1 Hz–10 kHz/0.5 A	300 s	<5 mΩ	3 A h 8s1p
NFC DC–AC	Multi-sine/PI[76]	0.01 Hz–4 kHz/—	—	—	800 V 2.6 A h
DC–AC	PI/LCL[53]	0.1–500 Hz/400 mA	—	<4.5%	8 A h 12s1p
DC–AC	PI + PR[77]	1–50 Hz/—	—	—	2.9 A h 8s1p
Active	S-Transform[78]	0.1 Hz–1 kHz/0.2–1.4 A cm^{-2}	—	<6%	90 kW fuel cell

reasonable disturbance current amplitudes to be designed for the corresponding equipment.[75,77] In short, these three scenarios have their own advantages and problems to be solved.

Additionally, attention should also be paid to selecting suitable control algorithms for specific control implementation. Although open-loop configurations combined with filtering elements (LC hardware filtering or DFT software filtering) can achieve sinusoidal perturbations for impedance measurements across battery terminals in certain scenarios, it is difficult for practical applications to maintain stable perturbation amplitudes and to avoid nonlinear distortion. The above difficulty significantly impedes the algorithm implementation in practical applications. Currently, perturbation schemes in various DC–DC circuits include half-bridge, full-bridge, DAB, TAB, and n-stage hybrid configurations, which predominantly employ conventional PI control strategies. Despite these strategies being effective in stabilizing routine DC, they might amplify noise for higher-frequency measurement due to the PI controller resonance under larger perturbation amplitude conditions. In order to address the above challenge, it is necessary to implement advanced control strategies such as PR controllers (enhancing specific frequency band tracking accuracy through resonant peaks) or d/q-axis transformation (converting AC quantities to DC quantities for decoupled control),[69,75] aiming at expanding the frequency response bandwidth and improving the measurement precision in the high-frequency range.

Besides, multi-sine perturbation and PRBS-like algorithms can significantly improve impedance measurement speed,[61,73] which are of great significance in monitoring the battery state.

A better understanding of section 2.3.1 can be realized by viewing the diagram in Fig. 3.

2.3.2 Distributed EIS. A distributed EIS system offers distinct advantages in battery diagnostics mainly because this architecture can generate AC perturbation signals with minimal interference ripple noise, and at the same time it can effectively compensate for inductive/resistive couplings.
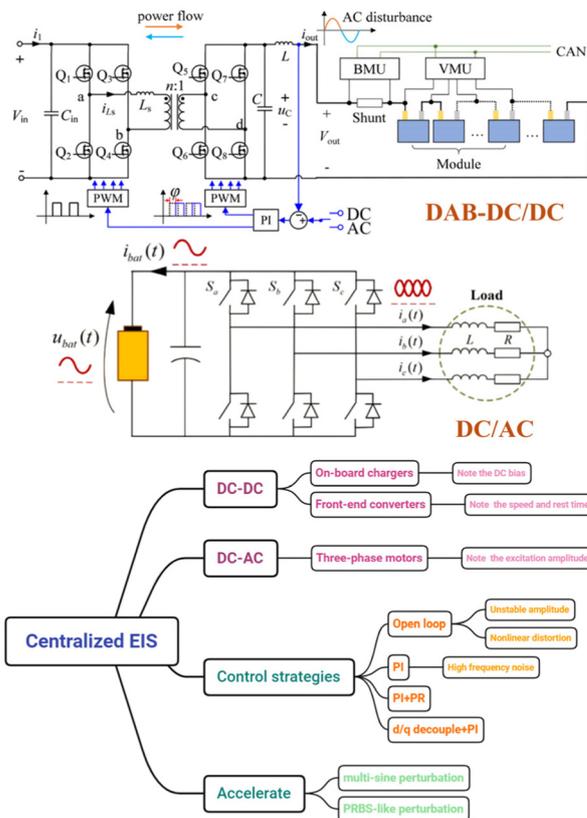
Fig. 3 A summary of centralized EIS scenarios and control strategies.[65,75]

Furthermore, the distributed EIS system can intelligently prioritize specific cells for targeted monitoring in practical applications, which offers a possibility to rapidly identify defective cells through screening protocols. However, the one-to-one correspondence between perturbation units and cells results in a significant scaling cost associated with peripheral circuitry when monitoring multi-cell battery packs.

The history of the distributed EIS system is not short in academic and industrial practice. The disturbance design of this system ranges from small DC–DC circuits[79] to equalization circuits,[80–82] and subsequently from an on-board BMS[83] to the chip-level.[84] Although there are differences in development methods and technical routes, the above efforts have collectively promoted the technological maturity and commercial application of the distributed EIS system.

It should be noted that the on-board acquisition of AC impedance is straightforward. A high-precision DAC functionality or switching control algorithm is required for integrated circuits or modules to generate and amplify various current perturbation waveforms through basic external components. A high-precision analog front-end (AFE) or equivalently expressed as an ADC can synchronously acquire voltage signals. The basic computational unit is capable of analyzing AC perturbation signals and calculating the single-frequency impedance. While these functional modules have been embedded into most microcontroller units (MCUs), practically, it is still a notable challenge to achieve fast impedance acquisition for lithium batteries with a low cost. The challenge is rooted in error analysis and compensation under multi-frequency perturbations, the synchronous control of voltage and current sampling, fast impedance calculation with noise reduction, and noise suppression and filtering control in measurement circuits. Usually, it is challenging to ensure the measurement accuracy of milliohm-level impedance that truly reflects the internal characteristics of the battery without prior design, specifically for AC impedance measurement. Currently, there are two commercially available distributed EIS chips for lithium batteries: the AD5941 chip from Analog Devices Inc.[85] and the DNB1168 chip from Datang NXP Co., Ltd.[86] Unlike the bulky and expensive potentiostats and electrochemical workstations, these chip-level solutions have fewer peripheral components, a smaller on-board size, and a lower cost.

The AD5941 high-precision low-power analog front-end measurement chip integrates a 16-bit successive approximation ADC (with dual sampling rates of 800 kSPS and 1.6 MSPS), a 12-bit high-speed DAC, a potentiostatic biasing module, a DFT-based AC impedance data processing engine and so on.[85] The company's related products include AD5933 (an earlier-generation product featuring a 12-bit ADC AFE), AD5940 (with different packaging), CN0510 (a single-cell EIS measurement system based on the AD5941 chip), and ADuCM355[87] (a system-in-package chip incorporating a Cortex-M3 core processor and the same AFE as AD5941). Besides, the newly launched battery pack management chip ADBMS2970 also supports EIS and boasts up to 20 voltage measurement channels.[88] If these specifications are validated, the first pack-level management chip with AC impedance modules will become true for lithium batteries. The application case of the AD5941 chip in related battery research is shown in Fig. 4.

In the official reference design for CN0510, the sinusoidal excitation signal is first generated using an on-chip waveform generator and 12-bit high-speed DAC, then amplified through an external Darlington transistor configuration, and finally
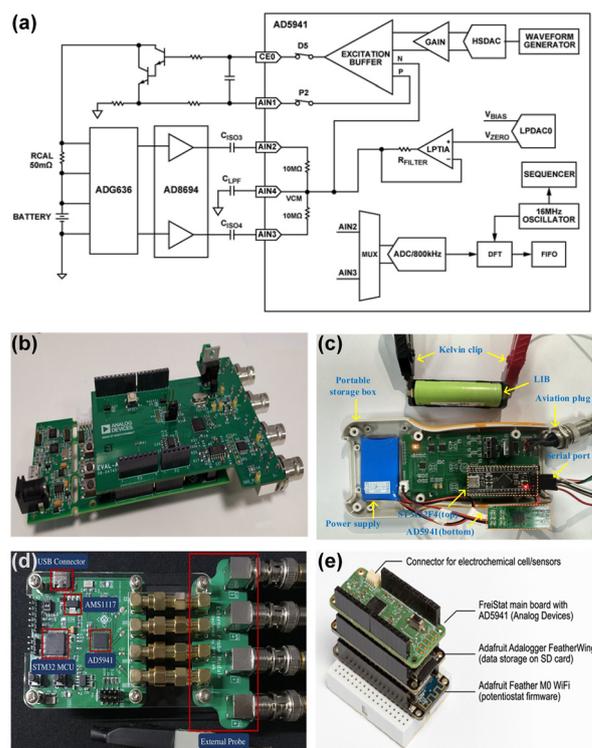

Fig. 4 The application cases of the AD5941 chip. (a and b) Official case CN0510;[85] (c) portable EIS device;[89] (d) cost-effective EIS device;[90] and (e) IoT-enabled device.[91]

applied to the battery. Before being routed to the ADC input pin for voltage measurement, the perturbation voltage is amplified using the gain amplifier AD8694, and parasitic capacitance is eliminated through the ADG636 multiplexer. After the amplitude and phase are extracted with the DFT module, battery impedance is calculated according to the calibration resistor R_{cal}:[85]

$$\dot{Z}_{\text{m}} = \left(\frac{\dot{V}_{Z_{\text{m}}}}{\dot{V}_{R_{\text{cal}}}}\right) \times R_{\text{cal}}. \qquad (5)$$

In other designs, in addition to modifying the original mechanical and circuit structure, Wu et al.[89] incorporated a differential amplifier, AD830, to construct a broadband constant current source with DC servo loop, generating a perturbation current signal with enhanced precision. Based on the above architecture, Tran et al.[90] developed a Qt-based interface. David Bill et al.[91] further integrated the system into the Arduino framework for developing AD5941 across various MCU platforms. All the above innovations have greatly promoted the progress of AC impedance measurement technology.

DNB1168 represents a cell-level battery management system based on the EIS monitoring functionality embedded in the integrated circuit. This chip integrates an on-chip temperature sensor for thermal monitoring except for voltage monitoring, SPI daisy-chain communication, cell balancing operations,

and so on.[86] Featuring a 14-bit ADC architecture, it implements current perturbation signals through external battery balancing circuits from 7.5 mHz to 7.8 kHz. The dedicated low-frequency noise suppression circuitry further enhances impedance measurement accuracy. For practical applications, flexible printed circuit (FPC) interconnects are adopted to enable direct contact with the cell negative terminal and busbar. This configuration not only improves the measurement precision of both temperature and impedance but also eliminates conventional sampling wires and connectors. Within the Datang NXP product family, EIS solutions include DNB1101 – optimized for energy storage systems – whereas DNB1168 targets vehicular environments with AEC-Q100 automotive-grade certification.[86] The relevant specific details are shown in Fig. 5.

The DNB1168 series supports SPI daisy-chaining with differential *I/O* interfaces, enabling single-chain expansion up to 250 chips while maintaining stable communication with minimal electromagnetic interference. Current academic reports primarily focus on the official evaluation boards of the DNB1168 series, with limited documentation on optimized improvements.[47,92–94] Nevertheless, partial production deployment has been achieved in industrial applications.

Definitely, distributed EIS solutions extend beyond the two aforementioned chips. For example, Young-Nam Lee *et al.*[95] developed EIS measurement systems using custom AFEs, FPGAs, and STM32 microcontrollers; Luigi Mattia *et al.*[83] implemented EIS battery pack measurements through FPGA and a battery management chip, L9963E; Bliss G. Carkhuff

Fig. 5 Relevant details of DNB1101/DNB1168.[47,86] (a) Chip connection schematic diagram; (b and c) official demo.

et al.[96] designed a Battery Internal Temperature Sensor-based BMS (BITS-BMS). Currently, the distributed EIS system mostly combines an on-chip internal signal generator and DAC to generate sinusoidal excitation signals. In the future, it is possible to generate multi-sine signals and PRBS-like signals with the corresponding processing algorithms for faster impedance measurement in practical applications.

3 Interpretation of impedance spectra

3.1 Acquisition of impedance spectra

For on-board battery impedance measurement based on single-frequency or multi-frequency perturbations, a low-pass or band-pass filter is used to smoothen the waveforms due to the limited resolution and conversion rate of the waveform generator. However, there is no ideal filter in reality; residual high-frequency noise, phase noise, and spectral leakage, all of them together will complicate the acquisition of AC impedance from voltage/current signals in the time domain. Accurate and efficient impedance extraction algorithms can significantly reduce measurement time and computational cost, thereby facilitating the development of its applications.

Currently, the two widely used impedance extraction algorithms are the multiplier scheme and the Fourier transform scheme. The multiplier scheme serves single-frequency sinusoidal perturbation and has quite a lot of advantages such as low computational cost, fast processing speed, and easy programming implementation. In addition, it can effectively suppress random white noise. However, when confronted with significant harmonic noise, its processing capability is insufficient, and if the temporal processing is not synchronized, it can introduce additional noise. The voltage response V_{ac} to an injection current $i_{ac} = a_0 \sin(\omega t)$ is expressed using the following equation:[97,98]

$$
\begin{aligned}
V_{ac} = a_0 |Z(\omega)| \sin(\omega t + \phi(\omega)) \\
+ \sum_m a_m \sin(m\omega t + \phi_m) + N(t)
\end{aligned}
\tag{6}
$$

where $|Z(\omega)|$ and $\phi(\omega)$ represent the modulus and initial phase angle of AC impedance $Z(\omega)$, respectively; a_m and ϕ_m denote the amplitude and initial phase angle of harmonic interference, respectively; and $N(t)$ indicates random interference noise. Then, the real and imaginary parts of the impedance $Z(\omega)$ can be obtained:

$$
\text{Re}(\omega) = \frac{1}{T} \int_0^T V_{ac}(t) \sin \omega t \, \mathrm{d}t
\tag{7}
$$

$$
\text{Im}(\omega) = \frac{1}{T} \int_0^T V_{ac}(t) \cos \omega t \, \mathrm{d}t.
\tag{8}
$$

Usually, the integral of random noise is assumed to be zero. If the harmonic interference can be neglected, substituting eqn (5) in eqn (6) and (7) yields:[97]
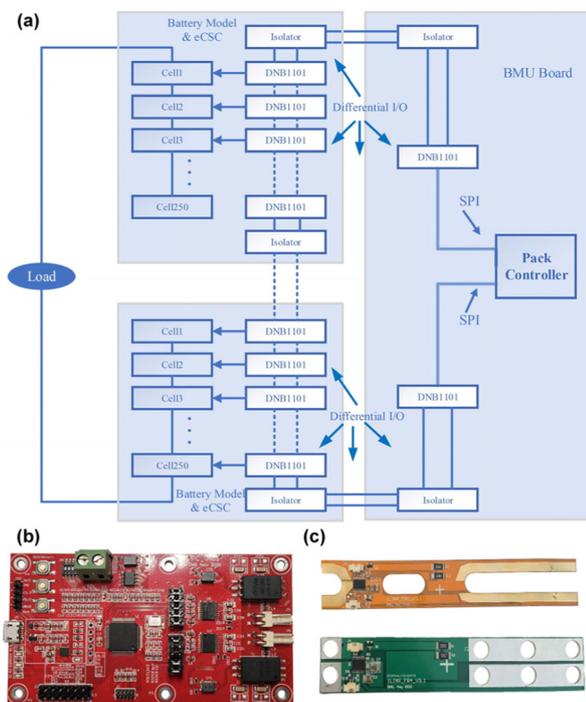
$$\mathrm{Re}(\omega) \approx a_0 |Z(\omega)| \cos \phi(\omega) \tag{9}$$

$$\mathrm{Im}(\omega) \approx a_0 |Z(\omega)| \sin \phi(\omega). \tag{10}$$

Eqn (8) and (9) indicate that under low harmonic interference conditions the real and imaginary parts of the impedance can be accurately obtained through the multiplier scheme based on the voltage signal in the time domain.

In contrast, the Fourier transform approach has undergone numerous methodological improvements during its development, such as Fast Fourier Transform (FFT), Short-Time Fourier Transform (STFT),[99] and Variable Window Fourier Transform. With these technical improvements, the Fourier transform approach not only can handle single-frequency disturbance but also acts as the basis for analyzing multi-frequency disturbance. The most significant feature of this approach is to effectively suppress high-frequency noise and accurately extract single-frequency impedance. Furthermore, high-efficiency Fourier transform embedded in various kernel modules has improved processing speed in practical applications. In FFT-based EIS measurement,[100] the aliased battery current $y_{\mathrm{I}}(t)$ combines DC offset, multi-frequency sinusoidal disturbances, and random noise. The resulting voltage response $y_{\mathrm{V}}(t)$ shares this structure. Both signals undergo Hanning windowing and optimization-based preprocessing before Fourier transform to derive $Y_{\mathrm{I}}(\omega)$ and $Y_{\mathrm{V}}(\omega)$. Impedance is then calculated as $Z(\omega) = Y_{\mathrm{V}}(\omega)/Y_{\mathrm{I}}(\omega)$, where the Hanning window mitigates spectral leakage in embedded systems.

$$y_{\mathrm{I}}(t) = I_0 + \sum_{n=1}^{10} I_n \sin(2\pi f_n t + \phi_{I_n}) + N_{\mathrm{I}}(t) \tag{11}$$

$$y_{\mathrm{V}}(t) = V_0 + \sum_{n=1}^{10} V_n \sin(2\pi f_n t + \phi_{V_n}) + N_{\mathrm{V}}(t) \tag{12}$$

$$w_{\mathrm{Hanning}}(n) = \begin{cases} 0.5\left[1 - \cos\left(2\pi \frac{n}{N}\right)\right], & 0 \le n \le N-1 \\ 0, & \mathrm{otherwise} \end{cases}. \tag{13}$$

The Fourier transform has inherent limitations, as it extracts the frequency components from the given signal but discards the specific time location. In addition to various windowing techniques, wavelet transform and S-transform have been developed to address the above limitations. These approaches introduce innovative basis functions, leading to the discrimination of frequency characteristics in impedance extraction. Li *et al.*[101] utilized the Complex Morlet Wavelet Transform (CMWT) to acquire and reconstruct impedance spectra in the frequency range of 0.1 Hz to 1 kHz. This method takes ~28 seconds and achieves average phase and amplitude errors of 2.6% and 0.7%, respectively. Geng *et al.*[102] employed Airy wavelet transform and Short Inverse Repeated Binary Sequence (SIRBS) injection to acquire impedance spectra in 10 seconds and achieved an average error of less than 1%. Besides, Yuan *et al.*[78] used the S-transform to achieve fast calculation of impedance spectra. Under square wave excitation, the average relative error is less than 3%. Compared with the Morlet wavelet transform, S-transform saves 95% of computed

time. In spite of excellent performance, these algorithms are still far away from practical application due to their complex implementations and computational requirements.

Other innovations in impedance acquisition include the filter design based on second-order generalized integrators (SOGIs)[103] and digital lock-in amplifiers (DLIAs) that incorporate second-order Hilbert transforms,[104] among others. These specialized designs can enhance the accuracy of impedance acquisition and reduce overall measurement time, and at the same time, they demonstrate strong feasibility in hardware implementation.

3.2 Validation of impedance spectra

Usually, the Kramers–Kronig transformation is used to assess the quality of the measured impedance data. The specific formulas are defined as follows:[105]

$$Z'(\omega) = \frac{2}{\pi} P \int_0^\infty \frac{\omega' Z''(\omega')}{\omega^2 - \omega'^2} \mathrm{d}\omega' \tag{14}$$

$$Z''(\omega) = -\frac{2\omega}{\pi} P \int_0^\infty \frac{Z'(\omega')}{\omega^2 - \omega'^2} \mathrm{d}\omega' \tag{15}$$

where P denotes the Cauchy principal value. Eqn (13) and (14) indicate that as long as the conditions of linearity, stability, causality and boundedness conditions are not violated, the real and imaginary parts of impedance spectra can be transformed into each other. The significant deviation from the Kramers–Kronig transformation might be attributed to the presence of nonlinear or non-stationary factors in the measurement process.

However, in practical impedance measurements, the limited frequency range will introduce inaccurate boundary initial values for the Kramers–Kronig transformation and will directly affect the validation accuracy. Additionally, to ensure the validation of the Kramers–Kronig transformation, the measurement density of the impedance spectra over the given frequency range must be high enough. To simplify the calculation, the linear Kramers–Kronig transformation (LKK) takes the place of the aforementioned validation. LKK is achieved by generalized linear equivalent circuit models, such as $R//C$ parallel configurations, to approximately assess the measurement error through fitting errors. The relevant formulas are expressed as follows:[106]

$$Z(\omega) \approx \hat{Z}_{\mathrm{LKK}}(\omega) = R_0 + \sum_{i=1}^{N} \frac{R_i}{1 + j\omega C_i R_i} \tag{16}$$

where R_0 denotes the ohmic resistance, while R_i and C_i represent the resistance and capacitance in each RC parallel element, respectively. In spite of the easy use for LKK, there may be overshoot and noise caused by an excessive number of RC elements due to the pre-defined equivalent circuit. To address this issue, at least two methods are presented. One is the iterative LKK,[105,107] which gradually increases the number of series RC components to avoid excessive order; the other is Tikhonov-regularized LKK (rLKK),[108] which introduces a regu-

larization penalty term to suppress noise in practical applications. In addition, constant phase elements (CPEs) and similar structures are also adopted in LKK. Although their impedance approaches infinity as the frequency tends to zero, which does not comply with the Kramers–Kronig relations, they may still fully adhere to the rules within the measurement range.[109]

The Kramers–Kronig transformation is very sensitive to violations of causality and stability, but it may have poor feedback regarding violations of linear conditions.[110–114] Using numerical simulations, Hirschorn *et al.*[115] revealed that the nonlinear response in electrochemical systems originates from the potential dependence of faradaic processes. Their findings highlight that the Kramers–Kronig relation can only be used to evaluate nonlinear behavior in systems with relatively high ohmic resistance. In other cases, the relation is not very sensitive. They define the ratio $R_{t,obs}/R_e$ and the characteristic frequency f_t. When the ratio $R_{t,obs}/R_e$ is small and the characteristic frequency f_t is below or close to the lower limit of the measurement range, nonlinear errors exceeding 4% violate the K–K relation. When these conditions are not met, the K–K relation is less sensitive to nonlinear errors.[116]

$$f_t = \frac{1}{2\pi R_{t,obs} C_{dl}} \left(1 + \frac{R_{t,obs}}{R_e} \right). \tag{17}$$

Some other studies[117,118] have also demonstrated the aforementioned findings and have assessed the linearity of real impedance spectra experimentally. The nonlinear responses were quantitatively evaluated with respect to sensitivity for three methods: Lissajous figures, total harmonic distortion (THD), and the Kramers–Kronig relationship. It was found experimentally that nonlinear distortion mainly occurs at mid to low frequencies, specifically below the frequency f_t. Lissajous figures show that nonlinear distortion is primarily manifested as changes in the shape and symmetry of the figures; however, it is a challenge for this method to determine the boundary points of nonlinearity. Regarding THD, random noise can be quantified through small perturbation harmonic analysis, but due to the heavy computation burden, it is difficult to establish accurate and universal numerical standards. In the experimental evaluation of the latter paper[118] for a nonlinear response of 20 mV$_{rms}$, the low-frequency Lissajous figure exhibited a distorted elliptical shape, and the low-frequency THD showed a significant increase exceeding 4%. In contrast, the Kramers–Kronig relationship was satisfied. It is only when the perturbation amplitude exceeds 60 mV$_{rms}$ do those violations of the Kramers–Kronig relationship occur due to its low sensitivity to nonlinearity.

Certainly, for single-frequency perturbation, the nonlinear effect can be mitigated by reducing the perturbation amplitude and applying data analysis techniques.[40] However, for multi-frequency perturbation, the measurement sensitivity to nonlinear effects is markedly reduced, while the influence of amplitude limitation is concurrently weakened. The lack of visualization of Lissajous figures, the decrease in Kramers–

Kronig validation sensitivity, and the increase in total harmonic distortion with ambiguous nonlinear characteristics collectively make the nonlinear assessment complex for multi-frequency perturbation. Furthermore, for the onboard impedance applications, verification after electrochemical measurement often fails to ensure that the battery state operating point is not affected by external interference. The study[112] revealed the potential invalidity of the Kramers–Kronig relationship for multi-sinusoidal perturbation, while THD analysis might amplify the parasitic nonlinearity from the external measurement artifact. The optimized Kramers–Kronig transformations or THD analysis combined with the device properties may be a feasible method for assessing the nonlinearity for multi-frequency perturbation in the future.

3.3 Analysis of impedance spectra

3.3.1 Analysis based on impedance models. Impedance characteristics are usually analyzed based on battery impedance models, mainly including electrochemical models and equivalent circuit models (ECMs). The electrochemical model consists of partial differential equations (PDEs) with initial and boundary conditions and involves electrode reaction kinetics and mass transport processes, where numerical methods are used to resolve impedance models.[119] In contrast, the equivalent circuit model is simple and easy to use due to its phenomenological characteristics. A recent breakthrough and development in electrochemical models is primarily in two directions: one is the physical–chemical coupling mechanism[119] and the other is to optimize the numerical solution.[120]

Regarding the development of electrochemical models, the research focus has gradually evolved from the early Single Particle Model (SPM)[120] to a multi-scale coupling framework. For instance, the Pseudo-Two-Dimensional Model (P2D)[121] enables dynamic simulation of solid–liquid phase reactions by integrating porous electrode theory, while the Transmission Line Model (TLM)[122] proposes an equivalent circuit description property for porous electrodes. Additionally, the classical Doyle–Fuller–Newman (DFN)[123] model establishes a unified analysis framework from particles to electrodes to cells. Moreover, Huang *et al.*[124] summarized the theoretical framework for the impedance response of porous electrodes. Similarly, Bai *et al.*[119] unified the DFN-like model under various physical scenarios using the complex phasor method in order to analyze the competitive mechanisms of charge transfer reactions. These developments and progress greatly improve the understanding of charge transfer reactions in batteries.

Regarding the computational efficiency of electrochemical models, model reduction techniques have been introduced, such as the extended single particle model, polynomial approximations, and Padé approximations.[125] These techniques allow for the typical impedance characteristics under specific conditions without sacrificing key dynamic characteristics. With the rapid development of computing power, electrochemical models have been increasingly applied in

various application scenarios. For example, the PyBaMM (Python Battery Mathematical Modeling) tool[126] employs a modular architecture design and matrix optimization techniques, reducing the basic computation time of traditional SPM, DFN models, and other physical–chemical coupling models to the millisecond level. It can be foreseen that electrochemical models will become increasingly accessible and comprehensively applied, extending from academic research to industrial applications.

Regarding the ECM method, the current focus is on how to optimize model structures and improve the reliability of parameter identification. In order to optimize the ECM structure, Warburg circuit elements are introduced to facilitate the transition from integer-order to fractional-order models. AI-based algorithms can be used to improve reliability and to accelerate the speed of parameter identification for ECMs. Table 3 summarizes the latest research development of ECMS. Some typical ECM structures expressed in circuit description codes (CDCs) are shown in Fig. 6.

Fitting impedance data to ECMs usually adopts the complex nonlinear least-squares algorithm and mainly relies on manually-operated platforms such as EQIVCT, ZView, ZSimpWin,[129] and PyEIS. The fitting accuracy generally depends on manually defined initial values and parameter locking procedures. With the rapid development of intelligent technologies, programming methods such as Python and MATLAB have accelerated automatic parameter identification, but their accuracy is still inferior to manual recognition in complex scenarios.

It must be emphasized that ECMs fail to characterize the intricate physicochemical processes in lithium-ion batteries, thereby limiting their practical applications. Luckily, the parameterization methodology marks a solid step forward in deeply understanding battery impedance characteristics.[119]

3.3.2 Analysis based on impedance deconvolution. It is not easy for us to quantitatively identify the parameters with physicochemical interpretability from the measured impedance spectra. Analyses of Nyquist plots or other graphical methods cannot reveal precise physicochemical meanings but some very general trends. The ECM-based method phenomenologically explains electrochemical processes; however this method requires a predefined circuit model. Consequently, prior knowledge-independent impedance reconstruction has
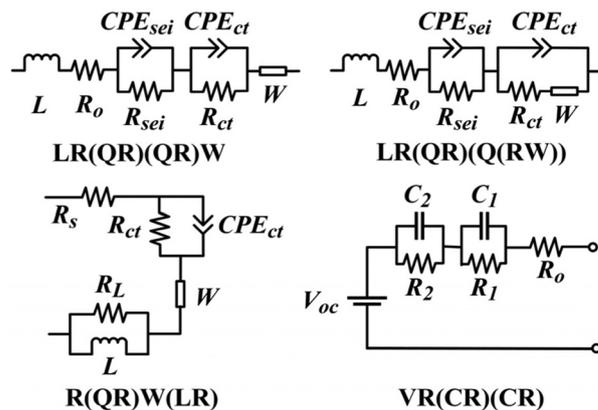

Fig. 6 Some typical equivalent circuit models for EIS data analysis.[127]

attracted growing attention. Among various reconstruction methods, the distribution of relaxation time (DRT) technique seems to be the most widely used.[137]

In essence, DRT analysis is to deconvolve frequency-domain data into time-domain relaxation time distribution functions $g(\tau)$. The logarithmic form of this function can be expressed as $\gamma(\tau) = \tau g(\tau)$. This expression enhances spectral resolution and electrochemical process separability. Its most prevalent mathematical expression is given as follows:[138]

$$Z(f) = R_o + R_p \int_0^\infty \frac{g(\tau)}{1 + i2\pi f\tau}\,\mathrm{d}\tau \tag{18}$$

$$Z(f) = R_o + R_p \int_0^\infty \frac{\gamma(\ln \tau)}{1 + i2\pi f\tau}\,\mathrm{d}\ln\tau \tag{19}$$

where R_o denotes the ohmic resistance, R_p denotes the total polarisation impedance, $\tau = RC$ denotes the time constant of the RC parallel circuit, and $g(\tau)$ conforms to a normal distribution with $\int_0^\infty g(\tau)\mathrm{d}\tau = 1$.

For non-ideal or fractional-order model elements such as Warburg elements and constant phase elements (CPEs), they can only be approximated by connecting in series a number of aggregate RC elements with different time constants and polarization strengths. For the inductance L parameter, with the time constant defined as t, it can be studied in generalized DRT (gDRT).[139,140]

Table 3 The method summary of equivalent circuit models for lithium ion batteries

Ref.	Model structure (CDC)	Fitting error	Identification method	Application scenario
128	Various circuits	—	CNLS	EQIVCT/manually
129	Various circuits	Chi-squares $10^{-3} < \chi^2 < 10^{-2}$ [130]	CNLS	ZsimpWin/manually
131	26 equivalent circuits	—	CNLS	Python environment
132	R(QR)W(LR)	$F_{\min} < 10^{-3}$	PRO	Optimization
130	Selected by machine learning	Chi-squares $10^{-2} < \chi^2 < 10^{-1}$ [130]	GOA	Automated processing
133	LR(QR)(QR)W	RMSE < 0.05	GSK	Dynamic conditions
134	LR(QR)(QR)W	RMSE 2.30%	Neural network	Automatic identification
135	CR(QR)	Success rate 0.875	Neural network	Automatic identification
127	LR(QR)(Q(RW))	MAPE 2.87%	Machine learning	AR-ECM/dynamic
136	VR(CR)(CR)	Min RMSE 4.893×10^{-3}	INFO	OCV estimation

Table 4 Comparison of the three common transformations

Characteristic	DRT	Fourier transform (FT)	Laplace transform (LT)
Base function type	Exponential decay function $e^{-t/\tau}$	Complex exponential $e^{-j\omega t}$	Damped complex exponential e^{-st}
Parameter space	Discrete relaxation time τ	Real frequency ω	Complex frequency $s = \sigma + j\omega$
Orthogonality	Nonorthogonal basis function	Orthogonal basis function	Nonorthogonal basis function
Integral kernel structure	$K(\omega,\tau) = \frac{1}{1+j\omega\tau}$	$K(t,\omega) = e^{-j\omega t}$	$K(t,s) = e^{-st}$
Complex plane coverage	Positive real axis τ	Imaginary axis ($\sigma = 0$)	Right half of the complex plane ($\sigma > \sigma_0$ convergence)
Inversion property	Conditionally unique (regularization-dependent)	Unique definite solution	Unique within the convergence region
Numerical stability	Sensitive to noise (require regularization)	Stability relies on signal truncation	High stability (damping factor suppresses noise)
Application scenario	EIS data processing	Frequency domain analysis	System stability analysis

From the mathematical perspective, DRT has similar properties to radial basis function expansion, and therefore can be compared and analyzed with common Fourier and Laplace transforms. The comparison results of the three transforms are shown in Table 4.

For DRT techniques, the exponential decay function $e^{-t/\tau}$ as the central mathematical model is used to describe the relaxation dynamics. However, the non-orthogonal basis function in DRT leads to the limitation in signal decomposition. Different from the orthogonal bases in Fourier transform, the inversion transform process is essentially a pathological inverse problem because there is a certain linear correlation between the basis groups of the exponential function in DRT. Therefore, it is difficult to fully deconvolute the exponential decay components corresponding to different time constants τ with the finite frequency-domain data, and the multiple inversions in the solution space might lead to a non-unique reconstruction for the relaxation time distribution function $g(\tau)$.

To address the aforementioned challenges, regularization methods (e.g., Tikhonov regularization,[141] ridge regression,[142] neural networks, etc.) are introduced to constrain the solution space and incorporate additional conditions through physical prior knowledge. The regularization method could stabilize inversion results and enhance resistance to noise interference.

However, this method potentially suppresses the contribution of signals with negative features. As a result, rigorous validation is necessary to prevent erroneous data interpretation due to regularization parameters. Most recently, the Bayesian probabilistic method was combined with the regularization method in order to improve back-convolution and confirm the optimal number of decoded peaks through prior knowledge and weighting matrices.[142] Nevertheless, these attempts require a trade-off between computational complexity and physical interpretation, and cannot overcome the theoretical bottleneck due to the lack of orthogonality. Nowadays, the traditional inversion transforms for DRT are shifting toward machine learning-assisted inversion algorithms. In the above intelligent inversion, deep neural networks are used to learn the implicit features of relaxation processes, which are just the limitations of traditional basis functions.

Table 5 summarizes various DRT decoding technologies with respect to the optimization method, fitting error, and application scenario.

Other deconvolution methods such as the Distribution of Capacitive Time (DCT)[154] and the Distribution of Differential Capacity (DDC)[145,155] have also regained attention. DCT first converts impedance data into admittance data, while DDC transforms complex impedance data into complex capacitance

Table 5 Comparison of various DRT decoding technologies for EIS

Ref.	DRT basic method	Optimization method	Fitting error	Application scenario
142	Ridge regression	Frequency analysis	—	Optimize regularization parameter
143	Tikhonov regularization	Shape factor co-analysis	MAE < 0.425	Optimize regularization parameter
144	Tikhonov regularization	Total outlier assessment	—	Quality-indicator-based preprocess
145	—	DRT/DDC symmetry analysis	—	Analyse the causes of pseudo-peaks
146	Hyper-λ algorithm/hierarchical Bayesian	Dual inversion framework/PFRT	—	Dual regression-classification framework/DRT valuation
147	Hierarchical Bayesian	Hyperparameter optimization	—	Bayesian estimation
148	Gaussian process	Hyperparameter optimization	—	Probabilistic method
149	Loewner framework	Linear systems theory	—	Without the regularization procedure
150	FFT-based DRT	—	$\varepsilon_\gamma = 2.04 \times 10^{-4}$	Time-domain DRT extraction
151	DNN/deep-DRT	Neural network deconvolution	—	Break the limits of regularisation
152	DNN-DRT	Neural network deconvolution	$\overline{\varepsilon_{\gamma,\text{DNN}}} \leq \overline{\varepsilon_{\gamma,\text{RR}}}$	For negative peak deconvolution
153	ANN-DRT	ANN-assisted prediction	R^2 0.9667	Only predict different DRT data

data. Subsequently, the same deconvolution operations as DRT are conducted to obtain the corresponding distribution functions. The formula expressions of related technologies are as follows:

$$\text{DCT}: Y(f) = 1/Z(f)$$
$$Y_{\text{DCT}}(f) = i2\pi f C_0 + G_0 + \int_{-\infty}^{+\infty} \gamma_{\text{DCT}}(\log \tau)\mathrm{d}\log\tau \tag{20}$$

$$\text{DDC}: C(\omega) = \frac{Q(\omega)}{U(\omega)} = \frac{I(\omega)}{j\omega U(\omega)} = \frac{1}{j\omega Z(\omega)}$$
$$C_{\text{DDC}}(\omega) = \int_0^{\infty} \frac{\gamma_{\text{DDC}}(\tau)}{1 + j\omega\tau}\mathrm{d}\tau \tag{21}$$

where C_0 and G_0 in the DCT formulation are the capacitance and conductance of the initial boundary,[154] the additional frequency-independent component C_0 is directly omitted in DDC, as it produces only a Dirac shock response δ under the voltage step, which is unobservable and does not affect the analysis of complex capacitance spectra.[155]

To complement the shortcoming of DRT technology, DCT and DDC are proposed, as defined above. Impedance spectra do not always converge at low frequencies, for example, solid–liquid diffusion impedance spectra for batteries. In this situation, DRT fails; however both DCT and DDC can directly deconvolute successfully. In addition, there is inherent symmetry between DRT and DDC methods, which includes the symmetry of the circuit structure, spectrum, deconvolution algorithm, and deconvolution results.[145] Our understanding of the relaxation time characteristics for batteries is still limited. Both DCT and DDC technologies can help us obtain more accurate relaxation time distribution functions and deepen our understanding of impedance reconstruction operations.

In summary, the distribution of relaxation time is very valuable, but it is still a challenge how to precisely deconvolute impedance spectra and how to exactly understand the deconvoluted results. Artificial intelligence assisted deconvolution techniques may provide better solutions to deconvolute impedance spectra and better understand the deconvoluted results.

4 Applications of impedance spectra

4.1 Battery state estimation

In order to fully utilize energy storage systems while ensuring their safety, their state estimation becomes crucial. Among the various states of batteries, the State of Charge (SOC) and the State of Health (SOH) might be the most important. The SOC can indicate the remaining capacity of the battery and prevent overcharging or over-discharging, and the SOH can indicate capacity degradation and identify deterioration patterns.

For the current battery management systems, the estimation of the SOC mainly relies on the compensated Coulomb counting method, and the estimation of the SOH mainly depends on the capacity degradation model. The compensation methods for SOC estimation typically include OCV model approaches or terminal voltage calibration at the end of

discharge, rooted in the SOC–OCV mapping relationship. The degradation model methods for SOH estimation are based on the impedance characteristics. Therefore, incorporating impedance spectra into state estimation is beneficial for the compensation of the Coulomb counting method and the construction of health indicators by improving the data-driven algorithm.

Table 6 gives a brief summary of SOC estimation and SOH prediction based on impedance spectra. It should be noted that most of the state estimation algorithms reported in the literature have not been validated in practical battery management systems. In detail, both accuracy and universality of the reported state estimation algorithms also need to be strictly verified in embedded environments.

There are still some differences in the estimation framework between the SOC and SOH. SOC estimation mainly aims at improving the accuracy of Coulomb counting by the real-time compensation based on circuit models. In contrast, SOH estimation aims at extracting health features from historical operational data based on the data-driven method. This difference is rooted in the fact that the SOC can rely on Coulomb counting results as a real-time baseline with inherent confidence, while SOH estimation lacks a similar real-time data anchor. In terms of methodology, SOC solutions emphasize lightweight algorithms for data processing and compensation, while SOH implementation requires extra computational resources for pattern recognition across battery datasets. In addition, SOC estimation requires a more stringent temporal resolution and is more sensitive to deviations of the identified parameters than SOH estimation.

In order to establish a stable mapping relationship between impedance features and the SOC for batteries, it is necessary to identify or extract impedance characteristics that are strongly correlated with the SOC but independent of the SOH, temperature, and other factors. However, AC impedance not only is a comprehensive reflection of the complex and coupled physicochemical processes inside batteries, but also extremely sensitive to the SOC. Therefore, it is difficult to standardize and generalize impedance characteristics to estimate the SOC and SOH of batteries. The open-circuit voltage (OCV) compensation method for SOC estimation affects the SOH, temperature, and relaxation processes. In contrast, impedance-based SOC estimation still has significant potential for application and accuracy advantages. With Pearson's r correlation matrix analysis on the LCO battery, Mc Carthy et al.[157] demonstrated that the impedance imaginary part at 10 Hz and the impedance real part at 2 Hz are very sensitive to the SOC. Furthermore, Buchicchio et al.[159] demonstrated that it is possible to estimate the SOC with a very sparse impedance spectra, and also demonstrated the potential application of lightweight machine learning algorithms. To some extent, impedance features can replace the OCV-based compensation methods for SOC estimation. Moreover, incorporating impedance characteristics into the OCV method can improve the accuracy of SOC estimation. If the impedance characteristics of fractional-order impedance models are incorporated, better SOC estimation

Table 6 Summary of impedance-based estimation of SOC and SOH for lithium-ion batteries

Ref.	Type	Estimation method	Estimation error	Scenario
156	SOC	Impedance Track algorithm compensated Coulomb counting	—	Embedded application
157	SOC	Pearson's r correlation matrix analysis	GOF 0.917	Theoretical analysis
158	SOC	Linear regression model and Gaussian process regression	<3.8%	Initial projections
159	SOC	Low-complexity machine learning based on the ECM	Accuracy 93.9%	Online application
160	SOC	Random forest combined with convolutional neural networks	R^2 0.9926	Small sample prediction
161	SOC	Fractional-order hysteresis thermoelectric coupling model	<2.5%	Wide temperature scene
162	SOC	Fractional-order adaptive square-root cubature Kalman filter	MAE < 0.5%	BMS application
163	SOC	Fractional-order multi-innovation unscented Kalman filter	RMSE 0.28%	BMS application
164	SOH	Fractional order modelling and analysis of relaxation effects	RMSE < 1%	Empirical method
165	SOH	Deep neural network transfer learning (DNN-TL)	R^2 0.9683	Data-driven scenario
166	SOH	1 kHz data interpolation and correlation analysis	PE 0.241%	Quick application
167	SOH	The ratio between the real part of 0.99 Hz and 1.976 Hz	MAPE 4.46%	Quick application
168	SOH	Automatic relevance determination and Gaussian process	—	Data-driven scenario
169	SOH	Convolutional autoencoder and deep neural network	RMSE 1.29%	Unsupervised application
170	SOH	Deep neural network transfer learning (DNN-TL)	MSE 0.1117	Prospective assessment
171	SOH	ECM with an added capacitor/Gaussian process regression	RMSE 1.77%	BMS application
172	SOH	DRT-CNN and gradient-weighted class activation mapping	R^2 0.9883	Embedded application
173	SOH	Simplified timescale information method and DRT	RMSE 1.36%	Real-time application

results can be obtained because fractional-order models are closer to the physical reality of batteries. For example, Chen *et al.*[162] and Zeng *et al.*[163] used fractional-order and Kalman filtering methods to significantly reduce the root mean square error of the SOC estimation results.

In early stages of impedance-based SOH estimation for batteries, researchers extracted initial features from raw impedance spectra based on the integer-order circuit model. Later, in order to derive more universal and widely applicable features, which can resist interference from other variables to a certain extent, complex fractional-order impedance models combined with DRT techniques are applied in machine learning algorithms and neural network models to extract impedance features. For example, Li *et al.*[171] constructed an equivalent circuit model with additional capacitance to improve the accuracy of impedance fitting and SOH estimation with Gaussian Process Regression (GPR). Kim *et al.*[172] used DRT to extract effective features, and train a compact Convolutional Neural Network (CNN) in embedded micro neural processing units. In spite of fewer parameters, their model demonstrated performance comparable to more complex models. Qian *et al.*[173] used a Gradient Boosting Decision Tree algorithm combined with Simplified Time Scale Information (STI) for data-driven SOH estimation, obtained strongly correlated STI features from raw data, multiple ECM structures, and DRT data, and finally achieved an average error of 1.36%. Obregon *et al.*[169] employed convolutional autoencoders (CAEs) to automatically extract features from impedance data, and subsequently, they used Deep Neural Networks (DNNs) to estimate the SOH, and finally, they achieved a maximum RMSE of 1.29% for test batteries. Fig. 7 summarizes four kinds of model frameworks for SOH estimation. The results suggest that most data-driven methods achieve excellent performance. These above frameworks improve the accuracy and applicability of SOH estimation, but a series of practical issues need further consideration, such as scale, computing power, and real-time. Currently, most data-driven state estimation models use uncorrelated features, whereas impedance spectra can reflect some intrinsic connections of physics. It is believed that the Physical Information Neural Network (PINN) established based on relevant features might promote better development of data-driven SOH estimation.[174]

Despite promising accuracy, data-driven SOC/SOH estimation faces four implementation barriers. First, complex models exceed the computational limits of affordable hardware, preventing real-time use. Second, models trained on limited datasets fail to generalize across battery types and aging conditions. Third, scarce full-lifecycle data hinder robust validation. Finally, slow multi-frequency EIS measurements conflict with real-time operational needs. Overcoming these requires lightweight algorithms, standardized datasets, and faster impedance techniques to bridge lab and practical applications.

4.2 Battery temperature estimation

It is insufficient to monitor the surface temperature of batteries for their diverse application scenarios. Therefore, it is crucial to detect the temperature inside batteries for ensuring their safe operation and long-term cycle life. In order to obtain reliable temperature inside the battery, researchers often use temperature estimation based on electrical signals or thermal models, where AC impedance and DC resistance play an important role. Temperature has a substantial impact on charge transfer reactions in the battery and, in turn, the evolution trend of charge transfer reactions with respect to temperature can be reflected by impedance spectra. Regarding impedance-based temperature estimation, early research is mainly focused on single frequency characteristics or ECM characteristics, while current research emphasizes the integration of impedance data with machine learning models and thermal models. Relevant studies for impedance-based temperature estimation are summarized in Table 7.

The single frequency impedance method aims to identify the feature which is not sensitive to parameters such as the
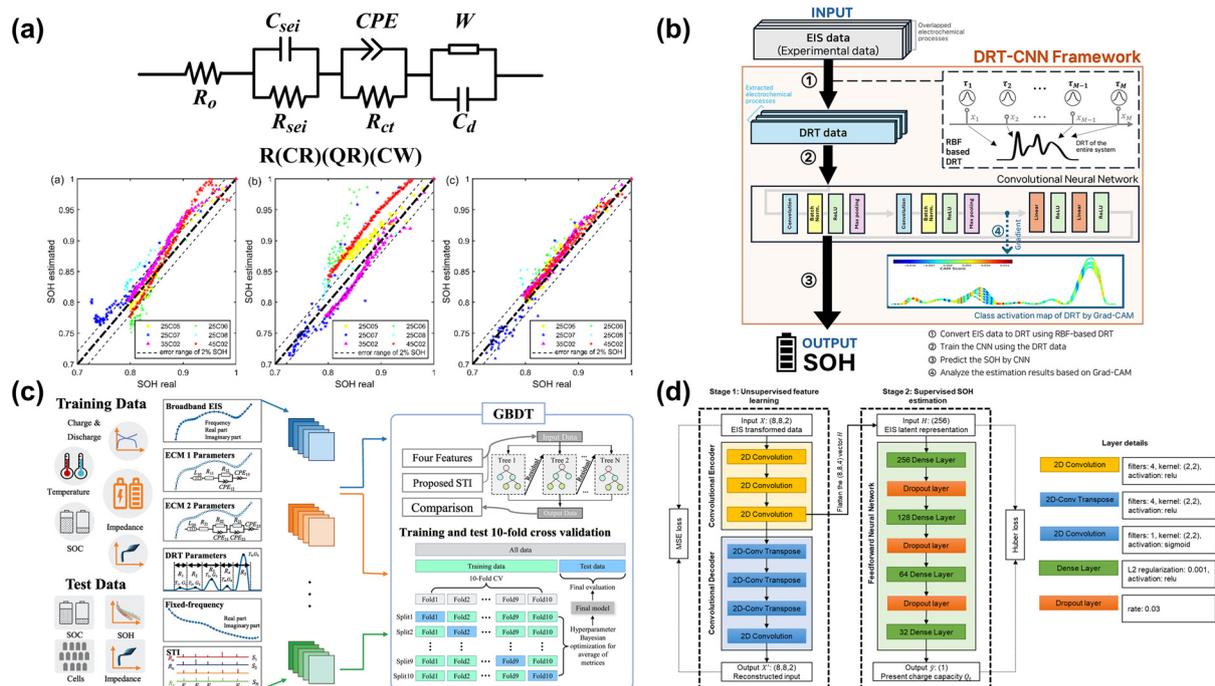
Fig. 7 Summary of four kinds of model frameworks for SOH estimation. (a) ECMC;[171] (b) DRT-CNN;[172] (c) STI-GBDT;[173] and (d) CAE-DNN.[169]

Table 7 A summary of temperature estimation methods based on EIS

Ref.	Type	Estimation method	Estimation error	Temperature range
175	Feature	The real part at 10.3 kHz/Arrhenius equation fitting	MAPE < 2.5 K	0–30 °C/transient
176	Feature	10\50\100 Hz phase shift/impedance matrix analysis	—	−10/20/50 °C
177	Feature	200 Hz impedance data/parametric fitting	RMSE 1.41 °C	10–55 °C
48	Feature	133 and 630 Hz impedance data/Monte Carlo simulations	MAPE ± 1 °C	−20–50 °C
178	Feature	Zero-crossing frequency f_{zero}/Newton–Raphson method	MAE 1.2 °C	−20–50 °C
179	Feature	10 Hz impedance data/Pearson correlation coefficient	RMSE 0.79 °C	0–60 °C
180	Feature	SEI layer impedance phase/DRT-based frequency selection	RMSE < 1%	−10–50 °C
181	Feature	The imaginary part at 600\800\1000 Hz/Arrhenius-like function	RMSE < 2.19 °C	−10–60 °C
182	Feature	850 mHz–3.15 kHz EIS data/least squares estimator	RMSE < 0.6 °C	−20–20 °C
183	Feature	The imaginary part at 26.83\273.27\377.45 Hz/GPR	RMSE < 1.12 °C	10–50 °C
184	Model	Voltage, current, and EIS data/multi-layer perceptron model	MAPE 1.086 °C	0–30 °C
185	Model	EIS data/DRT and six machine learning methods	MAE < 0.319 °C	0–30 °C
186	Model	EIS data/artificial neural networks (ANNs)	ΔT = 1 K	10–60 °C
187	Model	Voltage, current, and EIS data/LSTM-RNNs	RMSE < 0.46 °C	−20–50 °C
188	Model	Voltage, current, and the 215 Hz data/coupled electrothermal model	RMSE 0.23%	8–30 °C
189	Model	Voltage, current, and the pulse test/second-order RC ETCM	MAE 3.09%	15–45 °C
190	Model	$R_{\text{ohm}}\backslash R_{\text{ct}}\backslash\tau_d\backslash R_{\text{th}}\backslash\tau_{\text{th}}$ parameters/electrothermal model	MAPE $\leq$ 0.68 °C	0–50 °C
191	Model	Internal resistance/two-step resistance transfer algorithm (RTA)	MAPE < 1.515 °C	10–50 °C
192	Model	EIS data/fractional-order ECM and Kalman filter	MAPE < 1.5 °C	−30–80 °C
193	Model	Resistance entropy thermal model/digital twin framework	MAE < 0.73 °C	25–45 °C

SOC and SOH but sensitive to temperature. Due to the lack of the ability to fully decouple impedance spectra, extensive thermal tests are conducted to identify the relevant features. Furthermore, we cannot exclude all other environmental interferences in a compensatory manner.[119] Correlation analysis is usually used to select parameters for temperature estimations. For example, Pearson correlation coefficients or Spearman rank correlation indices can be used to assess the linear or monotonic relationships between impedance characteristics and temperature. The selected parameters require a sensitivity

analysis to quantify the temperature impact on them. For the identified feature parameters, application evaluation must be conducted under normal operating conditions to avoid potential influences from the testing environment. Because different batteries may have different formulations and materials, temperature estimation based on a single feature often lacks universality. The successful temperature estimation method for a certain type of battery may result in significant estimation errors when applied to other types of batteries. Ezahedi *et al.*[179] conducted a correlation analysis on a 70 A h large-

capacity battery and found a high sensitivity to temperature at 5–25 Hz and 250–1000 Hz and a low sensitivity to SOC/SOH at 10/20/25 Hz. The Gaussian regression model based on AC impedance at 10 Hz achieved an outstanding RMSE of 0.79 °C.

The core purpose of integrating impedance data into machine learning and thermal models is to construct a non-linear and multi-physics field framework for predicting temperature. Combining the impedance sensitivity with the non-linear modelling capability of machine learning algorithms, and at the same time, fusing the knowledge constraints from thermodynamic models, they can to some extent address the limitations of the dimensional perception of a single impedance feature. Regarding technical implementation, machine learning can be used to establish the nonlinear mapping relationship between impedance and temperature through supervised learning, and partial decoupling of interference factors can also be achieved through unsupervised learning. Regarding the electro-thermal coupled model, it mainly involves the ECM, full-order thermal model,[194] reduced-order lumped model, and thermal ECM. Among the above models, the single-cell thermal sub-model based on the lumped parameter model might be the most extensively used.[188]

Regarding machine learning, Liu et al.[184] extracted features of ECMs with Pearson analysis and principal component analysis. Based on inductance L, charge-transfer resistance R_{ct}, and double layer CPE parameters Y_0, n_0, they established multiple linear regression, Gaussian process regression, and multi-layer perceptron models. Chen et al.[185] used DRT to extract impedance features and found that the deconvoluted results have fewer outliers and are more stable models than the original impedance. Both Ströbel et al.[186] and Zheng et al.[187] validated the feasibility in using neural network models to estimate temperature. The ANN model constructed by the former[186] was concise, fast, and effective, while the latter[187] utilized operando impedance characteristics for real-time temperature estimation based on a long short-term memory recurrent neural network. Different from the classical static EIS, operando dynamic EIS was performed under the relaxed conditions and may violate the linearity and the smooth range.[187] Fig. 8 shows that both the real and imaginary parts of the operando dynamic EIS spectra are smaller than those of the classical static EIS spectra, but both exhibit the same trend of contracting towards the origin as the SOC increases. Regarding the above impedance spectra from these two measurement methods, the trend of the imaginary part and the phase angle are very similar with respect to the SOC; however, the real parts have a big difference. These results support the rationality of applying operando EIS for temperature detection.

Regarding electro-thermal coupling models, both Bai et al.[188] and Ma et al.[189] used a second-order RC thermal circuit model to simulate the cylindrical battery, while a three-dimensional multi-grid geometric thermal model was used to simulate the blade battery. Building on this foundation, Rodríguez-Iturriaga et al.[190] considered the heat generated by solid diffusion via ohmic resistance R_{ohm}, charge transfer resis-
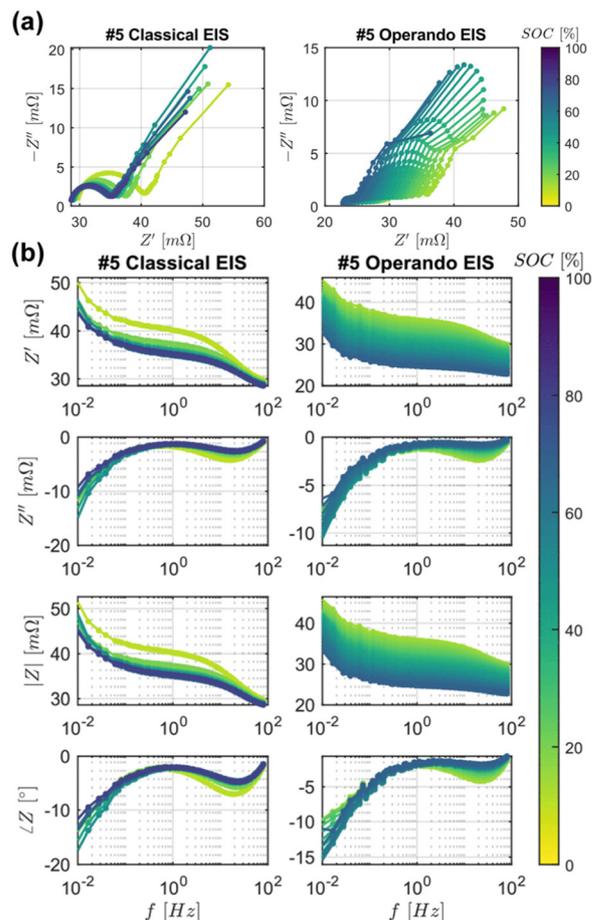

Fig. 8 Comparison between the classical static EIS and the operando dynamic EIS. (a) Nyquist diagram; (b) Bode diagram.[187]

tance R_{ct} and solid state diffusion characteristic time τ_d. The reduced-order thermal model provides some explanatory power for battery behaviors under conditions of different ambient temperatures and charge/discharge rates.

With a two-step resistance transfer algorithm, Xie et al.[191] established a thermal resistance network by replacing the lumped parameter model with a three-dimensional heat conduction equation. The presented method demonstrates superior computational speed compared to the finite element method and achieved an online value of 0.496 seconds for model computation. Based on fractional-order equivalent circuit models, Sun et al.[192] developed a frequency-domain distributed multi-point thermal model, in which the circuit model is in good agreement with the offline EIS analysis. This approach used a joint Kalman filter to achieve a joint estimation of tab temperature and time-varying thermal conductivity, with a maximum error of less than 1.5 °C. Currently, Shen et al.[193] integrated electro-thermal coupling models with deep learning technology. Based on experimental data, a finite element physical model was constructed to quantify the relationship between battery internal resistance and entropy production coefficient. After a convolutional neural network

was integrated into the above model, the temperature field distribution could be predicted with a mean absolute error of less than 0.73 °C within 2.92 seconds. The framework constructed for temperature distribution prediction is shown in Fig. 9.

While these advanced methods show promise, EIS-based temperature estimation faces unique challenges distinct from those in state estimation. A fundamental obstacle lies in decoupling the impedance response's inherent sensitivity to both temperature and state-of-health, as aging-induced degradation can mimic or mask thermal effects. Furthermore, the technique struggles with spatial resolution, providing a bulk internal value that may obscure critical localized hot spots. Translating lab-based models to real-world applications is also hindered by the complex heat transfer dynamics in battery packs, where cell-to-cell thermal interactions and cooling conditions significantly alter the core temperature–impedance relationship. Finally, achieving the required accuracy for safety-critical management under dynamic loads remains difficult, as transient conditions affect both the battery's thermal time constant and the impedance measurement itself.

4.3 Battery early safety warning

Early safety warning for batteries are extremely important, as there is often not enough time to issue warnings when thermal runaway occurs due to different reasons.[195] Current
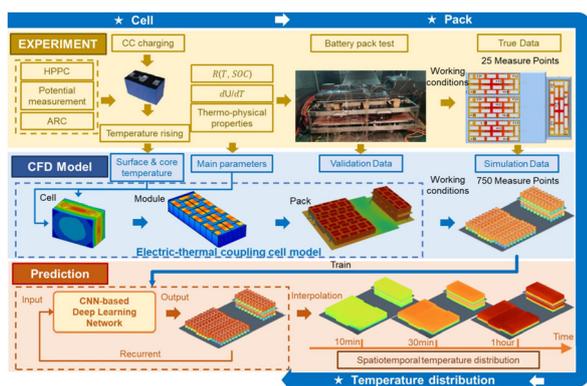

Fig. 9 Overview of a CNN-based framework for temperature distribution prediction from cell to pack.[193]

methods such as gas detection, surface temperature monitoring, internal short-circuit monitoring, and pressure detection generally fail to achieve perfect integration and information fusion. If overly reliant on a single data source, it may lead to false alarms or omissions in security alerts. Under normal operating conditions, frequent false alarms from the early warning system may actually lower the vigilance of management personnel, leading to more serious consequences. As a result, early warning systems not only require enough measured data related to thermal runaway caused by various misuse and abuse but also can integrate multidimensional data to reduce false alarm rates and issue warning signals earlier. On the one hand, EIS can reflect charge transfer reactions in batteries and can issue the early warning of thermal runaway; on the other hand, the advancement for impedance-based state estimation algorithms has significantly lowered the difficulty in integrating and processing impedance data. Safety warnings solely based on impedance features might cause false alarms, which could be addressed by multidimensional data fusion with impedance features. Impedance characteristics used to issue early warning for thermal runaway have been discussed above and a summary of it is listed in Table 8.

In the early warning for thermal runaway based on impedance characteristics, the single-frequency feature is primarily focused on phase declination[196] at specific frequencies or amplitude attenuation[197] under high-temperature conditions, while multi-frequency analyses are focused on the shrinkage or variation of impedance arcs in the low-frequency regime under high-temperature conditions. Regarding warning temperatures, the arc curve change or magnitude attenuation of impedance spectra is suitable to the thermal runaway warning at relatively low temperatures, typically between 60 and 80 °C,[201] while the phase and magnitude of impedance spectra transited from decreasing to increasing are suitable to the thermal runaway warning at middle temperatures, around 100 to 120 °C, which are regarded as the onset temperatures of thermal runaway in some situations. Furthermore, due to the minimal change in amplitude or phase of impedance spectra under thermal runaway conditions, single battery impedance monitoring is preferred for practical applications because the module-level impedance spectra often fail to monitor the thermal runaway. Impedance spectra are sampled at multiple

Table 8 Summary of thermal runaway warnings based on impedance characteristics

Ref.	Type	Impedance characteristics	Alarm temperature	Scenario
196	Single frequency	Impedance phase at 40 Hz	120 °C	TR test
197	Multi-frequency	The real part of EIS/ohmic resistance/ISC	—	Mechanical abuse
198	Single frequency	Dynamic impedance slope at 70 Hz	—	Overcharge
199	Multi-frequency	Full EIS data and DRT/DNN methods	—	ISC prediction
200	Multi-frequency	31.62 Hz phase/circular arc/linear slope	80 °C/120 °C/120 °C	ARC constant
201	Multi-frequency	EIS arc contraction or disappearance	55 °C	Pulse heating
202	Single frequency	Impedance amplitude at 0.1 Hz	82 °C/100 °C	Battery module
47	Single frequency	Impedance amplitude and phase at 1 kHz	45 °C/90 °C/fail T	ARC constant
203	Multi-frequency	Impedance phase at 200–600 Hz	45 °C	Charger
204	Single frequency	400.15 Hz phase < −0.5°/stabilized-phase $|Z|$ increase	55 °C/100 °C	ARC constant

dispersed mid-to-high frequency points for the purpose of capturing the dynamics of charge transfer reactions as fast as possible, and at the same time avoiding or mitigating false alarms inherent in single-frequency phase/amplitude methods. Nevertheless, these approaches may fail completely when addressing specific circuit failures such as conductor burnout or collector fracture induced by thermal runaway.[201] Current research mainly aims at utilizing the impedance technique to identify the cause or root of the thermal runaway, detect overcharging and lithium plating phenomena, and actively prevent and diagnose the risk of thermal runaway from the source.[198]

Conclusions

In spite of many challenges and uncertainties, the engineering and practical application of EIS-based state estimation and intelligent diagnosis of batteries are becoming increasingly clear. EIS-based battery management systems facilitate a deeper monitoring and understanding of the internal states of batteries under various operating conditions. Regarding practical applications, the technical roadmap for AC impedance includes at least three key nodes: miniaturization of measurement equipment, real-time data analysis, and accuracy of electrochemical models. These three key nodes play a critical role in achieving truly intelligent state monitoring and battery management systems. Currently, the progress of various impedance measurement schemes has nearly reached the first node of the technical roadmap for EIS-based intelligent diagnosis. Driven by artificial intelligence, continuous breakthroughs have been made in both real-time data analysis and the accuracy of electrochemical models. However, transforming EIS from a research tool into industrialized, large-scale applications still faces multiple challenges, including measurement robustness, model universality, and system integration. This requires multidisciplinary collaboration and standardization efforts to drive industrial implementation.

This paper comprehensively discusses EIS technology for batteries from three core aspects: AC impedance measurement, AC impedance data interpretation, and AC impedance applications.

(i) AC impedance measurement is focused on four potential sources of noise interference and centralized/distributed impedance measurement devices. Interferences such as crosstalk, DC bias, connection resistance, and ripple noise require certain considerations for impedance compensation. The design of impedance measurement equipment needs the consideration of different application scenarios in order to achieve higher speed and stability without sacrificing much accuracy.

(ii) The impedance data interpretation is focused on three key points: data acquisition, data validation, and data analysis, with emphasis on investigating data validation under various rapid measurement conditions and automatic processing of impedance data based on ECM models or DRT techniques.

(iii) How to understand impedance data for intelligent applications? Although uniquely designed impedance features perform well in some cases, further exploration in interpreting impedance data, innovative research on artificial intelligence algorithms, and theoretical development of thermoelectric coupling models, are still urgently needed in order to achieve better universality and interpretability.

In order to achieve breakthroughs in accuracy, efficiency, and intelligence for EIS-based battery management and thermal management strategies, multidimensional and systematic research and practice are required. Promising future development directions include establishing standardized EIS testing protocols and open impedance databases to facilitate comparative studies and accelerate model generalization. Integrating AI-driven interpretability frameworks with physical models will enhance the credibility and actionability of EIS-based diagnostics.[205,206] Ultimately, transitioning EIS from laboratory validation to field deployment requires industry endorsement and the development of new hardware platforms.

Author contributions

Y. Zhang developed the initial concept for this review. J. Xu and X. Xie contributed to conceptual discussion and refinement. Y. Zhang conducted extensive literature search and drafted the initial manuscript. Y. Zhang and J. Xu developed the methodology for analyzing the literature, created the figures and tables, and ensured the clarity and accuracy of the visual representation. Q. Huang modified the language and conducted thorough proofreading to ensure the manuscript's clarity and readability. Y. Zhang, Q. Huang, and J. Xie reviewed and revised the paper. J. Xie guided the research direction and critically reviewed and edited the manuscript. J. Xie proposed the systematic framework and provided overall supervision of this review.

Conflicts of interest

The authors declare no competing interests.

Abbreviations

ACMC	Average current-mode control
ADC	Analog to digital converter
AFE	Analog front end
ARC	Accelerating rate calorimetry
BMS	Battery management system
BTMS	Battery thermal management system
CMWT	Complex Morlet wavelet transform
CNLS	Complex nonlinear least squares
CPE	Constant phase element
DAB	Dual active bridge
DAC	Digital to analog converter
DCT	The distribution of capacitive time

DDC	The distribution of differential capacity
DFN	Doyle–Fuller–Newman
DFT	Discrete Fourier transform
DIBS	Discrete interval binary sequence
DLIA	Digital lock-in amplifier
DP	Discrete pulse
DRBS	Discrete random binary sequence
DRT	Distribution of relaxation time
ECM	Equivalent circuit model
EIS	Electrochemical impedance spectroscopy
EMF	Electromotive force
ERPGT	Evolutionary role-playing game theory
ESC	External short-circuit
ETCM	Electro-thermal coupling model
FBG	Fiber Bragg grating
FFT	Fast Fourier transform
FIBC	Floating-interleaving boost converter
GOA	Global optimization algorithm
GPR	Gaussian process regression
GSK	Gaining-sharing knowledge metaheuristic algorithm
INFO	Innovative weighted mean of vectors
IOT	Internet of things
ISC	Internal short-circuit
LCOE	Levelized cost of electricity
LKK	Linear Kramers–Kronig
LSTM	Long short-term memory
MAPE	Mean absolute percentage error
MCU	Microcontroller unit
MSE	Mean square error
NTC	Negative temperature coefficient
OBC	On-board charger
P2D	Pseudo-two-dimensional model
PDE	Partial differential equation
PE	Percentage error
PFRT	Probability function of relaxation time
PHM	Prognostics and health management
PI	Proportional integral
PR	Proportional resonant
PRBS	Pseudo-random binary sequence
PRO	Partial reinforcement optimizer
PSC	Phase shift control
PWM	Pulse width modulation
RMSE	Root mean square error
RTA	Resistance transfer algorithm
RTD	Resistance temperature detector
SEI	Solid-electrolyte interphase
SIRBS	Short inverse repeated binary sequence
SNR	Signal-to-noise ratio
SOC	State of charge
SOGI	Second-order generalized integrator
SOH	State of health
SPM	Single particle model
SPS	Samples per second
STFT	Short-time Fourier transform
TAB	Triple-active-bridge
THD	Total harmonic distortion
TLM	Transmission line model
TR	Thermal runaway

Data availability

No primary research results, software or codes have been included and no new data have been generated or analysed as part of this review.

Acknowledgements

References

1 M. Deehan, I. Renta, S. Yaary, J. Fillingham, S. Sarkar, G. Matlock, L. Newcomb, E. Bayler, J. Ghirardelli and M. Grasso, 2023 NOAA Science Report, 2024, DOI: 10.25923/x0x7-f622.

2 D. Raimi and R. G. Newell, *Resources for the Future*, Washington, DC, USA, 2024, https://www.rff.org/publications/reports/global-energy-outlook-2023.

3 D. Raimi, Y. Zhu, R. G. Newell and B. C. Prest, *Resources for the Future*, Washington, DC, USA, 2024, https://www.rff.org/publications/reports/global-energy-outlook-2024.

4 D. Yang, Y. Lv, M. Ji and F. Zhao, *Int. J. Low-Carbon Technol.*, 2024, **19**, 18–23.

5 A. Hamdan, C. D. Daudu, A. Fabuyide, E. A. Etukudoh, S. Sonko and J. World, *Adv. Res. Rev.*, 2024, **21**, 1984–1998.

6 H. Song, C. Liu, A. M. Amani, M. Gu, M. Jalili, L. Meegahapola, X. Yu and G. Dickeson, *Energy and AI*, 2024, **17**, 100378.

7 H. Niu, N. Zhang, Y. Lu, Z. Zhang, M. Li, J. Liu, W. Song, Y. Zhao and Z. Miao, *J. Energy Storage*, 2024, **88**, 111666.

8 M. Lecompte, J. Bernard, E. Calas, L. Richardet, A. Guignard, F. Duclaud, D. Voyer, M. Montaru, B. Crouzevialle and L. Lonardoni, *J. Energy Storage*, 2024, **94**, 112443.

9 Y. Li, J. Li, Y. Ding, X. Feng, X. Liu, P. Yan, M. Sui and M. Ouyang, *Energy Storage Mater.*, 2024, **65**, 103167.

10 D. Ouyang, J. Weng, J. Hu, J. Liu, M. Chen, Q. Huang and J. Wang, *J. Electrochem. Soc.*, 2019, **166**, A559.

11 X. Feng, M. Ouyang, X. Liu, L. Lu, Y. Xia and X. He, *Energy Storage Mater.*, 2018, **10**, 246–267.

12 J. Fan, C. Liu, N. Li, L. Yang, X.-G. Yang, B. Dou, S. Hou, X. Feng, H. Jiang and H. Li, *Nature*, 2025, **641**, 639–645.

13 J. B. Robinson, M. Maier, G. Alster, T. Compton, D. J. Brett and P. R. Shearing, *Phys. Chem. Chem. Phys.*, 2019, **21**, 6354–6361.

14 B. Gulsoy, T. Vincent, J. Sansom and J. Marco, *J. Energy Storage*, 2022, **54**, 105260.

15 F. Ren, T. Cox and H. Wang, *J. Power Sources*, 2014, **249**, 156–162.

16 X. Feng, X. He, M. Ouyang, L. Wang, L. Lu, D. Ren and S. Santhanagopalan, *J. Electrochem. Soc.*, 2018, **165**, A3748–A3765.

17 H. Wang, E. Lara-Curzio, E. T. Rule and C. S. Winchester, *J. Power Sources*, 2017, **342**, 913–920.

18 Y. Xiao, F. Yang, Z. Gao, M. Liu, J. Wang, Z. Kou, Y. Lin, Y. Li, L. Gao and Y. Chen, *J. Energy Storage*, 2023, **64**, 107145.

19 X. Feng, S. Zheng, D. Ren, X. He, L. Wang, H. Cui, X. Liu, C. Jin, F. Zhang and C. Xu, *Appl. Energy*, 2019, **246**, 53–64.

20 Y. Y. Kee, Y. Asako, T. L. Ken and N. A. C. Sidik, *J. Adv. Res. Fluid Mech. Therm. Sci.*, 2020, **68**, 54–62.

21 D. Chen, Q. Zhao, Y. Zheng, Y. Xu, Y. Chen, J. Ni and Y. Zhao, *Sensors*, 2023, **23**, 5609.

22 A. Raghavan, P. Kiesel, L. W. Sommer, J. Schwartz, A. Lochbaum, A. Hegyi, A. Schuh, K. Arakaki, B. Saha and A. Ganguli, *J. Power Sources*, 2017, **341**, 466–473.

23 A. Ganguli, B. Saha, A. Raghavan, P. Kiesel, K. Arakaki, A. Schuh, J. Schwartz, A. Hegyi, L. W. Sommer and A. Lochbaum, *J. Power Sources*, 2017, **341**, 474–482.

24 M. Zwicker, M. Moghadam, W. Zhang and C. Nielsen, *J. Adv. Join. Process*, 2020, **1**, 100017.

25 P. Lyu, X. Liu, C. Liu and Z. Rao, *Int. J. Heat Mass Transfer*, 2023, **211**, 124279.

26 R. R. Richardson, P. T. Ireland and D. A. Howey, *J. Power Sources*, 2014, **265**, 254–261.

27 W. Ma, Y. Xie, S. Guo, W. Li, R. Yang, S. Panchal and Y. Zhang, *J. Energy Storage*, 2024, **102**, 114066.

28 M. E. Orazem and B. Tribollet, *ChemTexts*, 2020, **6**, 12.

29 A. C. Lazanas and M. I. Prodromidis, *ACS Meas. Sci. Au*, 2023, **3**, 162–193.

30 F. Single, B. Horstmann and A. Latz, *J. Phys. Chem. C*, 2019, **123**, 27327–27343.

31 Z. Chen, D. L. Danilov, R. A. Eichel and P. H. Notten, *Adv. Energy Mater.*, 2022, **12**, 2201506.

32 X. Wang, X. Wei, J. Zhu, H. Dai, Y. Zheng, X. Xu and Q. Chen, *eTransportation*, 2021, **7**, 100093.

33 K. Mc Carthy, H. Gullapalli, K. M. Ryan and T. Kennedy, *J. Electrochem. Soc.*, 2021, **168**, 080517.

34 D. Qu, W. Ji and H. Qu, *Commun. Mater.*, 2022, **3**, 61.

35 P. Iurilli, C. Brivio and V. Wood, *J. Power Sources*, 2021, **505**, 229860.

36 W. Hu, Y. Peng, Y. Wei and Y. Yang, *J. Phys. Chem. C*, 2023, **127**, 4465–4495.

37 V. Vivier and M. E. Orazem, *Chem. Rev.*, 2022, **122**, 11131–11168.

38 X. Du, J. Meng, Y. Amirat, F. Gao and M. Benbouzid, *J. Energy Chem.*, 2024, **95**, 464–483.

39 N. Meddings, M. Heinrich, F. Overney, J.-S. Lee, V. Ruiz, E. Napolitano, S. Seitz, G. Hinds, R. Raccichini and M. Gaberšček, *J. Power Sources*, 2020, **480**, 228742.

40 J. R. Macdonald, W. B. Johnson, I. Raistrick, D. Franceschetti, N. Wagner, M. McKubre, D. Macdonald, B. Sayers, N. Bonanos and B. Steele, *Impedance spectroscopy: theory, experiment, and applications*, John Wiley & Sons, 2018.

41 J. R. Macdonald, *Ann. Biomed. Eng.*, 1992, **20**, 289–305.

42 W.-h. Li, Q.-a. Huang, W.-m. Yang, C.-p. Yang and J.-j. Zhang, *J. Electrochem.*, 2020, **26**, 10.

43 W. Choi, H.-C. Shin, J. M. Kim, J.-Y. Choi and W.-S. Yoon, *J. Electrochem. Sci. Technol.*, 2020, **11**, 1–13.

44 S. S. Zhang, K. Xu and T. Jow, *Electrochim. Acta*, 2006, **51**, 1636–1640.

45 I. Santos-Mendoza, J. Vázquez-Arenas, I. González, G. Ramos-Sánchez and C. Castillo-Araiza, *Int. J. Chem. React. Eng.*, 2019, **17**, 20180095.

46 X. Wang, X. Wei, J. Zhu, H. Dai, Y. Zheng, X. Xu and Q. Chen, *eTransportation*, 2021, **7**, 100093.

47 Y. Li, L. Jiang, N. Zhang, Z. Wei, W. Mei, Q. Duan, J. Sun and Q. Wang, *J. Energy Chem.*, 2024, **92**, 74–86.

48 H. Beelen, K. Mundaragi Shivakumar, L. Raijmakers, M. Donkers and H. J. Bergveld, *Int. J. Energy Res.*, 2020, **44**, 2889–2908.

49 J. P. Christophersen, W. H. Morrison, J. L. Morrison, C. G. Motloch and D. M. Rose, IEEE Aerospace Conference, 2012, pp. 1–16.

50 L. Raijmakers, K. M. Shivakumar, M. Donkers, M. Lammers and H. Bergveld, *IFAC-PapersOnLine*, 2016, **49**, 42–47.

51 L. Raijmakers, Delft University of Technology, 2018, ISBN 978-94-6228-861-4.

52 M. Oldenburger, B. Beduerftig, A. Gruhle, F. Grimsmann, E. Richter, R. Findeisen and A. Hintennach, *J. Energy Storage*, 2019, **21**, 272–280.

53 X. Wei, X. Wang and H. Dai, *Energies*, 2018, **11**, 64.

54 E. Karden, S. Buller and R. W. De Doncker, *J. Power Sources*, 2000, **85**, 72–78.

55 M. J. Brand, E. I. Kolp, P. Berg, T. Bach, P. Schmidt and A. Jossen, *J. Energy Storage*, 2017, **12**, 45–54.

56 M. J. Brand, P. A. Schmidt, M. F. Zaeh and A. Jossen, *J. Energy Storage*, 2015, **1**, 7–14.

57 C. Bolsinger, M. Zorn and K. P. Birke, *J. Energy Storage*, 2017, **12**, 29–36.

58 A. Y. Kallel and O. Kanoun, *J. Energy Storage*, 2023, **58**, 106267.

59 F. M. Janeiro, Y. Hu and P. M. Ramos, *Measurement*, 2020, **150**, 107040.

60 Z. Guo, Q. Wang, W. Yang, M. Hu, G. Wang, D. Lu, M. Bai and C. Lyu, *2022 17th ICIEA*, 2022, 1252–1256.

61 Z. Liu, X. Wang, G. Chang, H. Yuan, W. Tang, X. Wei and H. Dai, *IEEE Trans. Power Electron.*, 2024, **39**, 16826–16838.

62 J. Sihvo, D.-I. Stroe, T. Messo and T. Roinila, *IEEE Trans. Power Electron.*, 2019, **35**, 2548–2557.

63 J. Sihvo, T. Roinila and D.-I. Stroe, *IEEE Trans. Ind. Electron.*, 2020, **68**, 4916–4926.

64 S. A. Assadi, Z. Gong, C. F. Wang, J. Piruzza, J. Xu, D. Jokic, S. Sarofim and O. Trescases, *2022 IEEE APEC*, 2022, 1056–1063.

65 X. Wang, X. Wei, Q. Chen and H. Dai, *IEEE Trans. Ind. Electron.*, 2020, **68**, 7380–7390.

66 H. H. Abbasali and S. J. Ashtiani, *IEEE Trans. Instrum. Meas.*, 2022, **71**, 1–8.

67 J. A. A. Qahouq and Z. Xia, *IEEE Trans. Ind. Electron.*, 2017, **64**, 7019–7029.

68 S. R. Islam and S.-Y. Park, *IEEE Trans. Ind. Appl.*, 2019, **56**, 1661–1669.

69 J. Shen, H. Homayouni and J. Wang, *IEEE Trans. Ind. Electron.*, 2020, **68**, 8819–8828.

70 O. M. Faloye and P. Barendse, *2019 IEEE ECCE*, 2019, 2682–2689.

71 S. K. Dam and V. John, *IEEE Trans. Ind. Appl.*, 2017, **54**, 1502–1512.

72 J. Sha, X. Li and G. Qiu, *IEEE Trans. Power Electron.*, 2024, **39**, 14167–14171.

73 K. Zhang, R. Xiong, S. Qu, B. Zhang and W. Shen, *IEEE Trans. Transp. Electrif.*, 2024, 1–1, DOI: 10.1109/tte.2024.3362992.

74 V.-T. Doan, V.-B. Vu, H.-N. Vu, D.-H. Tran and W. Choi, *2015 9th ICPE-ECCE Asia*, 2015, 1644–1649.

75 H. Qu, D. Luo, D. Jiang, M. Zhou, X. Zhao and W. Sun, *IEEE Trans. Power Electron.*, 2025, **40**, 3490–3504.

76 K.-P. Liu, G. Orfanoudakis, S. M. Sharkh and A. Cruden, *2023 IEEE 14th SDEMPED*, 2023, 606–612.

77 H. Qu, B. Li, M. Zhou, D. Jiang and W. Sun, *ICPE 2023-ECCE Asia*, 2023, 3138–3143.

78 H. Yuan, R. Du, X. Wang, X. Wei and H. Dai, *IEEE Trans. Ind. Electron.*, 2022, **70**, 3740–3750.

79 L. Wang, X. Zeng, L. Chen, L. Lv, L. Liao and J. Jiang, *J. Electrochem. Energy Convers. Storage*, 2025, **22**, 011008.

80 E. Din, C. Schaef, K. Moffat and J. T. Stauth, *IEEE Trans. Power Electron.*, 2016, **32**, 5688–5698.

81 P.-H. La and S.-J. Choi, *2021 IEEE APEC*, 2021, 975–980.

82 G. Chen, W. Liu, S. Wang, K. Yang, Z. Song and J. Meng, *2024 21st ICHQP*, 2024, 236–241.

83 L. Mattia, G. Petrone, F. Pirozzi and W. Zamboni, *J. Energy Storage*, 2024, **81**, 110330.

84 N. Datang, *Battery Management IC (DNB1168)*, 2014.

85 AD5941 product description, https://www.analog.com/en/products/ad5941.html.

86 DNB1168 product description, https://www.datangnxp.com/details/products/43.

87 ADuCM355 product description, https://www.analog.com/en/products/aducm355.html.

88 ADBMS2970 product description, https://www.analog.com/en/products/adbms2970.html.

89 J. Wu, W. Bai, L. Zhang, X. Zhang, H. Lin, H. Dai, J. Liu, F. Zhang and Y. Yang, *J. Energy Storage*, 2024, **84**, 110856.

90 N. L. Tran, N. Q. Ha-Phan, T. L. Phan, C. T. S. Ching and M. K. Ha, *IEEJ Trans. Electr. Electron. Eng.*, 2024, **19**, 1730–1736.

91 D. Bill, M. Jasper, A. Weltin, G. A. Urban, S. J. Rupitsch and J. Kieninger, *Anal. Chem.*, 2023, **95**, 13003–13009.

92 L. Wang, X. Zhao, Z. Deng and L. Yang, *J. Energy Storage*, 2023, **57**, 106275.

93 Q. Li, D. Yi, G. Dang, H. Zhao, T. Lu, Q. Wang, C. Lai and J. Xie, *World Electr. Veh. J.*, 2023, **14**, 321.

94 G. Huang and X. Zhu, *2024 9th ICETIS*, 2024, 144–147.

95 Y.-N. Lee, S.-W. Jo, G. Rahim, S.-G. Lee and K. Kwon, *IEEE Trans. Ind. Electron.*, 2025, **72**, 3202–3212.

96 B. G. Carkhuff, P. A. Demirev and R. Srinivasan, *IEEE Trans. Ind. Electron.*, 2018, **65**, 6497–6504.

97 H. Homayouni, J. DeVaal, F. Golnaraghi and J. Wang, *IEEE Trans. Transp. Electrif.*, 2018, **4**, 418–431.

98 *Impedance Spectroscopy: Theory, Experiment, and Applications*, ed. E. Barsoukov and J. R. Macdonald, John Wiley & Sons Inc.: Hoboken, NJ, 2005.

99 D. Klotz, M. Schönleber, J. P. Schmidt and E. Ivers-Tiffée, *Electrochim. Acta*, 2011, **56**, 8763–8769.

100 P. Lu, M. Li, L. Zhang and L. Zhou, *2019 PHM-Qingdao*, 2019, 1–6.

101 W. Li, Q.-A. Huang, C. Yang, J. Chen, Z. Tang, F. Zhang, A. Li, L. Zhang and J. Zhang, *Electrochim. Acta*, 2019, **322**, 134760.

102 A. Geng, H. Hu, Z. Zhao, J. Chen, Y. Ge, K. Wang and Z. He, *IEEE Trans. Transp. Electrif.*, 2024, **11**, 2444–2455.

103 S. Fan, Z. Li, C. Yu, D. Li, Y. Zhang, D. Wen and Z. Shao, *IEEE Trans. Power Electron.*, 2024, **39**, 10675–10681.

104 Y.-N. Lee, K-S. Choi, S.-W. Jo, G. Rahim, K. Kwon and S.-G. Lee, *2023 I2MTC*, 2023, 1–6.

105 M. Schönleber, D. Klotz and E. Ivers-Tiffée, *Electrochim. Acta*, 2014, **131**, 20–27.

106 J. Luo, X. Liang, Y. Zhang, C. Liang, H. Yassine, G. Leroy, J.-C. Carru and M. Mascot, *J. Solid State Electrochem.*, 2021, **25**, 2225–2233.

107 V. Yrjänä and J. Bobacka, *Electrochim. Acta*, 2024, **504**, 144951.

108 A. Y. Kallel and O. Kanoun, *2021 IWIS*, 2021, 7–10.

109 F. Fasmin and R. Srinivasan, *J. Solid State Electrochem.*, 2015, **19**, 1833–1847.

110 M. A. Zabara, C. B. Uzundal and B. Ulgut, *J. Electrochem. Soc.*, 2019, **166**, A811.

111 R. Reséndiz, A. Rodríguez, E. Larios, J. Torres, F. Castañeda and R. Antaño-López, *J. Electroanal. Chem.*, 2022, **904**, 115879.

112 C. You, M. A. Zabara, M. E. Orazem and B. Ulgut, *J. Electrochem. Soc.*, 2020, **167**, 020515.

113 K. J. Szekeres, S. Vesztergom, M. Ujvári and G. G. Láng, *ChemElectroChem*, 2021, **8**, 1233–1250.

114 G. Katırcı, F. E. Civan, S. Jung, C. B. Lee and B. Ülgüt, *Electrochim. Acta*, 2024, **481**, 143984.

115 B. Hirschorn and M. E. Orazem, *J. Electrochem. Soc.*, 2009, **156**, C345.

116 B. Hirschorn, B. Tribollet and M. E. Orazem, *Isr. J. Chem.*, 2008, **48**, 133–142.

117 J. J. Giner-Sanz, E. Ortega and V. Pérez-Herranz, *Electrochim. Acta*, 2015, **186**, 598–612.

118 J. M. Goh, C. Eluagu, J. Babauta and M. E. Orazem, *J. Electrochem. Soc.*, 2024, **171**, 036508.

119 Y. Bai, Q.-A. Huang, K. Wu and J. Zhang, *J. Energy Chem.*, 2024, **92**, 759–798.

120 N. Hallemans, N. E. Courtier, C. P. Please, B. Planden, R. Dhoot, R. Timms, D. Howey and S. R. Duncan, *J. Electrochem. Soc.*, 2025, **172**, 060507.

121 M. Pathak, M. D. Murbach, C. Pathak, T.-J. Jang, Y. Qi, D. T. Schwartz and V. R. Subramanian, *J. Electrochem. Soc.*, 2018, **165**, A1324.

122 X. Kong, G. L. Plett, M. S. Trimboli, Z. Zhang and Y. Zheng, *J. Electrochem. Soc.*, 2020, **167**, 013539.

123 J. Zhao and J. A. A. Qahouq, *Next Energy*, 2024, **5**, 100153.

124 J. Huang, Y. Gao, J. Luo, S. Wang, C. Li, S. Chen and J. Zhang, *J. Electrochem. Soc.*, 2020, **167**, 166503.

125 H. A. A. Ali, L. H. Raijmakers, K. Chayambuka, D. L. Danilov, P. H. Notten and R.-A. Eichel, *Electrochim. Acta*, 2024, **493**, 144360.

126 V. Sulzer, S. G. Marquis, R. Timms, M. Robinson and S. J. Chapman, *J. Open Res. Softw.*, 2021, **9**, 1.

127 Q. You, Y. Zhang, R. Xiong and H. Ruan, *J. Electrochem. Soc.*, 2025, **172**, 020518.

128 B. A. Boukamp, *Solid State Ionics*, 1986, **20**, 31–44.

129 B. Yeum, *Ann Arbor, Michigan, USA (1999–2005)*, 1999.

130 Z. Zhao, Y. Zou, P. Liu, Z. Lai, L. Wen and Y. Jin, *Electrochim. Acta*, 2022, **418**, 140350.

131 K. B. Knudsen, *ECS Meeting Abstracts*, 2019, **235**, 1937–1937.

132 A. AbdelAty, M. E. Fouda, A. Elwakil and A. Radwan, *J. Electrochem. Soc.*, 2024, **171**, 050553.

133 H. Nunes, J. Martinho, J. Fermeiro, J. Pombo, S. Mariano and M. do Rosário Calado, *IEEE Trans. Ind. Appl.*, 2024, **60**, 5048–5060.

134 J. Wang, B. Jiang, Y. Ou, X. Wang, X. Wei and H. Dai, *2024 ITEC Asia-Pacific*, 2024, 978–983.

135 Q. Hua and M. Shen, *2023 IEEE NorCAS*, 2023, 1–6.

136 W. Merrouche, B. Lekouaghet, E. Bouguenna and Y. Himeur, *J. Energy Storage*, 2024, **76**, 109891.

137 A. Maradesa, B. Py, J. Huang, Y. Lu, P. Iurilli, A. Mrozinski, H. M. Law, Y. Wang, Z. Wang and J. Li, *Joule*, 2024, **8**, 1958–1981.

138 Y. Lu, C.-Z. Zhao, J.-Q. Huang and Q. Zhang, *Joule*, 2022, **6**, 1172–1198.

139 C. Plank, T. Rüther, L. Jahn, M. Schamel, J. P. Schmidt, F. Ciucci and M. A. Danzer, *J. Power Sources*, 2024, **594**, 233845.

140 M. A. Danzer, *Batteries*, 2019, **5**, 53.

141 T. H. Wan, M. Saccoccio, C. Chen and F. Ciucci, *Electrochim. Acta*, 2015, **184**, 483–499.

142 P. Carbone, A. De Angelis, A. Bertei, A. Maradesa and F. Ciucci, *J. Electrochem. Soc.*, 2025, **172**, 020533.

143 J. Wang, Q.-A. Huang, J. Wang and J. Zhang, *J. Electroanal. Chem.*, 2024, **962**, 118272.

144 N. Schlüter, T. Bergmann, S. Ernst and U. Schröder, *ChemElectroChem*, 2021, **8**, 1167–1182.

145 J. Wang, Q.-A. Huang, W. Li, J. Wang, Y. Bai, Y. Zhao, X. Li and J. Zhang, *J. Electroanal. Chem.*, 2022, **910**, 116176.

146 J. Huang, N. P. Sullivan, A. Zakutayev and R. O'Hayre, *Electrochim. Acta*, 2023, **443**, 141879.

147 F. Ciucci and C. Chen, *Electrochim. Acta*, 2015, **167**, 439–454.

148 J. Liu and F. Ciucci, *Electrochim. Acta*, 2020, **331**, 135316.

149 A. Sorrentino, B. Patel, I. V. Gosea, A. C. Antoulas and T. Vidaković-Koch, *J. Power Sources*, 2023, **585**, 233575.

150 B. Py and F. Ciucci, *J. Electrochem. Soc.*, 2025, **172**, 026504.

151 E. Quattrocchi, T. H. Wan, A. Belotti, D. Kim, S. Pepe, S. V. Kalinin, M. Ahmadi and F. Ciucci, *Electrochim. Acta*, 2021, **392**, 139010.

152 E. Quattrocchi, B. Py, A. Maradesa, Q. Meyer, C. Zhao and F. Ciucci, *Electrochim. Acta*, 2023, **439**, 141499.

153 X. Liu, Z. Yan, J. Wu, J. Huang, Y. Zheng, N. P. Sullivan, R. O'Hayre, Z. Zhong and Z. Pan, *J. Energy Chem.*, 2023, **78**, 582–588.

154 B. Py, A. Maradesa and F. Ciucci, *Electrochim. Acta*, 2024, **479**, 143741.

155 M. Schönleber and E. Ivers-Tiffée, *Electrochem. Commun.*, 2015, **61**, 45–48.

156 Texas Instruments BQ40Z50, https://www.ti.com/product/BQ40Z50.

157 K. Mc Carthy, H. Gullapalli, K. M. Ryan and T. Kennedy, *J. Energy Storage*, 2022, **50**, 104608.

158 I. Babaeiyazdi, A. Rezaei-Zare and S. Shokrzadeh, *Energy*, 2021, **223**, 120116.

159 E. Buchicchio, A. De Angelis, F. Santoni, P. Carbone, F. Bianconi and F. Smeraldi, *Energy*, 2023, **283**, 128461.

160 X. Zhang, L. Zhang, J. Wu, W. Bai, H. Dai, H. Lin, F. Zhang and Y. Yang, *J. Electroanal. Chem.*, 2025, 119093.

161 J. Zeng, S. Wang, P. Takyi-Aninakwa, M. Zhang, W. Cao, C. Fernandez and J. M. Guerrero, *Int. J. Circuit Theory Appl.*, 2025, **53**, 655–680.

162 L. Chen, W. Yu, G. Cheng and J. Wang, *Energy*, 2023, **271**, 127007.

163 J. Zeng, S. Wang, M. Zhang, W. Cao, C. Fernandez and J. M. Guerrero, *J. Energy Storage*, 2024, **86**, 111283.

164 M. Messing, T. Shoa and S. Habibi, *J. Energy Storage*, 2021, **43**, 103210.

165 I. Babaeiyazdi, A. Rezaei-Zare and S. Shokrzadeh, *IEEE Trans. Transp. Electrif.*, 2022, **9**, 886–895.

166 K. Mc Carthy, H. Gullapalli and T. Kennedy, *Appl. Energy*, 2022, **307**, 118210.

167 Z. Pang, K. Yang, Z. Song, P. Niu, G. Chen and J. Meng, *J. Energy Storage*, 2023, **72**, 108693.

168 J. Wang, R. Zhao, Q.-A. Huang, J. Wang, Y. Fu, W. Li, Y. Bai, Y. Zhao, X. Li and J. Zhang, *J. Power Sources*, 2023, **561**, 232737.

169 J. Obregon, Y.-R. Han, C. W. Ho, D. Mouraliraman, C. W. Lee and J.-Y. Jung, *J. Energy Storage*, 2023, **60**, 106680.

170 Y. Li, M. Maleki and S. Banitaan, *J. Energy Storage*, 2023, **73**, 109185.

171 C. Li, L. Yang, Q. Li, Q. Zhang, Z. Zhou, Y. Meng, X. Zhao, L. Wang, S. Zhang and Y. Li, *J. Energy Storage*, 2024, **86**, 111167.

172 K. Kim, K. Park, K. Yoon, H. Moon, H. Pyeon, J. Kim and S. Han, *J. Power Sources*, 2025, **631**, 236169.

173 G. Qian, Y. Zheng, X. Li, Y. Sun, X. Han and M. Ouyang, *Appl. Energy*, 2025, **382**, 125272.

174 Y. Luo, S. Ju, P. Li and H. Zhang, *Electrochim. Acta*, 2025, **525**, 146110.

175 J. P. Schmidt, S. Arnold, A. Loges, D. Werner, T. Wetzel and E. Ivers-Tiffée, *J. Power Sources*, 2013, **243**, 110–117.

176 J. Zhu, Z. Sun, X. Wei and H. Dai, *J. Power Sources*, 2015, **274**, 990–1004.

177 K. Mc Carthy, H. Gullapalli and T. Kennedy, *J. Power Sources*, 2022, **519**, 230786.

178 A. A. Hussein and A. A. Fardoun, *IEEE Trans. Ind. Appl.*, 2020, **56**, 3043–3051.

179 S. E. Ezahedi, M. Kharrich and J. Kim, *J. Energy Storage*, 2024, **94**, 112467.

180 S. S. Bhoir, G. Thenaisie, C. Brivio and M. Paolone, *J. Energy Storage*, 2024, **97**, 112754.

181 A. Geng, H. Hu, J. Chen, Y. Ge and Z. He, *IEEE Trans. Power Electron.*, 2025, **40**, 6454–6458.

182 X. Du, J. Meng, J. Peng, Y. Zhang, T. Liu and R. Teodorescu, *IEEE Trans. Power Electron.*, 2022, **37**, 10101–10105.

183 J. Li, T. Li, Y. Qiao, Z. Tan, X. Qiu, H. Deng, W. Li, X. Qi and W. Wu, *J. Energy Storage*, 2025, **118**, 116287.

184 Y. Liu, L. Yang, R. Liao, C. Hu, Y. Xiao, J. Wu, C. He, Y. Zhang and S. Li, *J. Energy Storage*, 2024, **87**, 111426.

185 X. Chen, Q. Li, B. Shao, W. Dou, C. Lai, T. Lu and J. Xie, *Energy*, 2025, **320**, 135493.

186 M. Ströbel, J. Pross-Brakhage, M. Kopp and K. P. Birke, *Batteries*, 2021, **7**, 85.

187 Y. Zheng, Y. Che, J. Guo, N. A. Weinreich, A. Kulkarni, A. Nadeem, X. Sui and R. Teodorescu, *IEEE Trans. Power Electron.*, 2024, **39**, 13853–13868.

188 W. Bai, X. Zhang, Z. Gao, S. Xie, K. Peng and Y. Chen, *Int. J. Energy Res.*, 2023, **2023**, 4021256.

189 X. Ma, Y. Zhang, R. Liu, P. Chang, D. Li, G. Bai and S. Liu, *Appl. Therm. Eng.*, 2025, **269**, 126063.

190 P. Rodríguez-Iturriaga, V. M. García, S. Rodríguez-Bolívar, E. E. Valdés, D. Anseán and J. A. López-Villanueva, *Appl. Energy*, 2024, **367**, 123327.

191 Y. Xie, W. Ma, W. Li, R. Yang, X. Hu, Y. Luo and Y. Zhang, *IEEE Trans. Power Electron.*, 2025, **40**, 7453–7465.

192 Y. Sun, Z. Zhang, Y. Jin, R. Cao, B. Xu, X. Liu and S. Yang, *Int. J. Heat Mass Transfer*, 2024, **235**, 126157.

193 K. Shen, Y. Ling, X. Meng, X. Lai, Z. Zhu, T. Sun, D. Li, Y. Zheng, H. Wang and C. Xu, *J. Energy Storage*, 2025, **113**, 115676.

194 S. Ludwig, M. Steinhardt and A. Jossen, *Batteries*, 2022, **8**, 60.

195 Y. Dai and A. Panahi, *Next Energy*, 2025, **6**, 100186.

196 R. Srinivasan, P. A. Demirev and B. G. Carkhuff, *J. Power Sources*, 2018, **405**, 30–36.

197 M. Spielbauer, P. Berg, M. Ringat, O. Bohlen and A. Jossen, *J. Energy Storage*, 2019, **26**, 101039.

198 N. Lyu, Y. Jin, R. Xiong, S. Miao and J. Gao, *IEEE Trans. Ind. Electron.*, 2021, **69**, 1929–1936.

199 B. Cui, H. Wang, R. Li, L. Xiang, J. Du, H. Zhao, S. Li, X. Zhao, G. Yin and X. Cheng, *J. Power Sources*, 2023, **563**, 232824.

200 P. Dong, Z. Liu, P. Wu, Z. Li, Z. Wang and J. Zhang, *J. Electrochem. Soc.*, 2021, **168**, 090529.

201 S. Yang, X. Wang, S. Zhou, Y. Zhuang, H. Jin, J. Chen, J. Liu, Z. Gao, X. Zhou and Q. Wang, *J. Energy Storage*, 2024, **99**, 113393.

202 L. Torres-Castro, A. M. Bates, N. B. Johnson, G. Quintana and L. Gray, *J. Electrochem. Soc.*, 2024, **171**, 020520.

203 J. Ning, B. Xiao and W. Zhao, *Eng. Rep.*, 2025, **7**, e13082.

204 J. Perez, E. Garayalde, J. Lorente, M. Arrinda, M. Oyarbide, H. Macicior, U. Iraola and H. J. Grande, *Int. J. Electr. Power Energy Syst.*, 2025, **171**, 111053.

205 Y. Bai, Q.-A. Huang, Z. Wu, J. Wang, J. Chen, K. Wu and J. Zhang, *J. Energy Chem.*, 2025, **107**, 939–979.

206 Z. Wu, Q.-A. Huang, Y. Bai, J. Zhang and K. Wu, *J. Energy Chem.*, 2025, **112**, 1026–1045.